



**HAL**  
open science

## Confocal Volumetric $\mu$ XRF and Fluorescence Computed $\mu$ -Tomography Reveals Arsenic Three-Dimensional Distribution within Intact *Pteris vittata* Fronds

Antony van Der Ent, Martin D de Jonge, Kathryn Spiers, Dennis Brueckner, Emmanuelle Montargès-Pelletier, Guillaume Echevarria, Xiaoming Wang, Mei Lei, Rachel Mak, James Lovett, et al.

### ► To cite this version:

Antony van Der Ent, Martin D de Jonge, Kathryn Spiers, Dennis Brueckner, Emmanuelle Montargès-Pelletier, et al.. Confocal Volumetric  $\mu$ XRF and Fluorescence Computed  $\mu$ -Tomography Reveals Arsenic Three-Dimensional Distribution within Intact *Pteris vittata* Fronds. *Environmental Science and Technology*, 2020, 54 (2), pp.745-757. 10.1021/acs.est.9b03878 . hal-02401572

**HAL Id: hal-02401572**

**<https://hal.science/hal-02401572>**

Submitted on 16 Nov 2020

**HAL** is a multi-disciplinary open access archive for the deposit and dissemination of scientific research documents, whether they are published or not. The documents may come from teaching and research institutions in France or abroad, or from public or private research centers.

L'archive ouverte pluridisciplinaire **HAL**, est destinée au dépôt et à la diffusion de documents scientifiques de niveau recherche, publiés ou non, émanant des établissements d'enseignement et de recherche français ou étrangers, des laboratoires publics ou privés.

1           **Confocal volumetric  $\mu$ XRF and fluorescence computed**  
2            **$\mu$ -tomography reveals arsenic three-dimensional distribution**  
3           **within intact *Pteris vittata* fronds**

4  
5           Antony van der Ent<sup>1,2\*</sup>, Martin D. de Jonge<sup>3</sup>, Kathryn M. Spiers<sup>4</sup>, Dennis Brueckner<sup>4,5,6</sup>,  
6           Emmanuelle Montargès-Pelletier<sup>7</sup>, Guillaume Echevarria<sup>2</sup>, Xiao-Ming Wan<sup>8</sup>, Mei Lei<sup>8</sup>,  
7           Rachel Mak<sup>9</sup>, James Lovett<sup>10</sup>, Hugh H. Harris<sup>10\*</sup>

8  
9                           <sup>1</sup>Centre for Mined Land Rehabilitation, Sustainable Minerals Institute,  
10                           The University of Queensland, Australia.

11  
12                           <sup>2</sup>Laboratoire Sols et Environnement, UMR 1120, Université de Lorraine, France.

13  
14                           <sup>3</sup>Australian Synchrotron, ANSTO, Australia.

15  
16                           <sup>4</sup>Photon Science, Deutsches Elektronen-Synchrotron DESY, Germany.

17  
18                           <sup>5</sup>Department of Physics, University of Hamburg, Germany.

19  
20                           <sup>6</sup>Faculty of Chemistry and Biochemistry, Ruhr-University Bochum, Germany.

21  
22                           <sup>7</sup>Laboratoire Interdisciplinaire des Environnements Continentaux, CNRS - Université de Lorraine, France.

23  
24                           <sup>8</sup>Center for Environmental Remediation, Institute of Geographic Sciences and Natural Resources Research,  
25                           Chinese Academy of Sciences, China.

26  
27                           <sup>9</sup>Department of Chemistry, University of Sydney, Australia.

28  
29                           <sup>10</sup>Department of Chemistry, The University of Adelaide, Australia.  
30  
31

32 **ABSTRACT**

33 The fern *Pteris vittata* has been the subject of numerous studies because its extreme arsenic  
34 hyperaccumulation characteristics. However, information on the arsenic chemical speciation and  
35 distribution across cell types within intact frozen-hydrated *Pteris vittata* fronds is necessary to better  
36 understand the arsenic biotransformation pathways in this unusual fern. While 2D X-ray absorption  
37 spectroscopy imaging studies show that different chemical forms of arsenic – As(III) and As(V) –  
38 occur across the plant organs, depth-resolved information of arsenic distribution and chemical  
39 speciation in different cell types within tissues of *Pteris vittata* have not been reported. By using a  
40 combination of planar and confocal  $\mu$ -X-ray fluorescence imaging and fluorescence computed  $\mu$ -  
41 tomography, this study reveals the localization of Arsenic in the endodermis and pericycle  
42 surrounding the vascular bundles in the rachis and the pinnules of the fern. Arsenic is also  
43 accumulated in the vascular bundles connecting into each sporangium, and in some mature sori. The  
44 use of 2D X-ray absorption near edge structure imaging allows for deciphering arsenic speciation  
45 across the tissues, revealing arsenate in the vascular bundles and arsenite in the endodermis and  
46 pericycle. This study demonstrates how different advanced synchrotron X-ray microscopy  
47 techniques can be complementary in revealing, at tissue and cellular levels, elemental distribution  
48 and chemical speciation in hyperaccumulator plants.

49

50 **Keywords:** *chemical speciation; elemental distribution; hyperaccumulator; fern.*

51

52

## 53 1. INTRODUCTION

54 Hyperaccumulator plants are able to regulate potentially toxic concentrations of trace elements in  
55 their living tissues<sup>1,2,3</sup>. Arsenic hyperaccumulation has been described for a number of pteridophytes  
56 (ferns) from the genus *Pteris* (Pteridaceae), most notably *Pteris vittata*, which accumulates up to  
57 22 600  $\mu\text{g g}^{-1}$  As<sup>4,5</sup> and *Pityrogramma calomelanos* which accumulates up to 16 400  $\mu\text{g g}^{-1}$  As<sup>6,7</sup> in  
58 fronds. Phytoextraction with *P. vittata* has been successfully applied in the remediation of soil and  
59 groundwater As<sup>8,9,10</sup>. The As hyperaccumulation mechanisms of *P. vittata* have elicited intensive  
60 research<sup>11,12,13,14</sup>. Arsenic content in *P. vittata* follows the order of pinnae > stipe > root, with most  
61 As distributed in the pinnae (78–96%). The concentration of As in the pinnae decreases from the  
62 base to the apex of the fronds, and As concentrations in midribs is much lower than in the pinnae<sup>15</sup>.  
63 The As concentration was relatively high in the midrib compared to the surrounding tissues, and  
64 there could be an unloading process of As from midrib to mesophyll tissues<sup>16</sup>. An interesting finding  
65 is that As concentrations in spores were far lower than in the pinnae, indicating that *P. vittata* tends  
66 to keep As away from reproductive organelles<sup>15</sup>. At the cellular level, energy dispersive X-ray  
67 spectroscopy combined to scanning electron microscopy (SEM-EDS) identified that As is primarily  
68 distributed within the upper and lower epidermis of the pinna in *P. vittata*<sup>15</sup>. Analysis with X-ray  
69 fluorescence imaging ( $\mu\text{XRF}$ ) led to the reporting of even higher As concentration in trichomes  
70 compared that prevailing As concentrations in the epidermis<sup>17</sup>. At the subcellular level, As was  
71 mainly stored in the cytoplasmic supernatant fraction, accounting for 78% of As in the pinnae<sup>18</sup>.  
72 Therefore, As compartmentalisation in trichomes and vacuoles was suggested as a detoxification  
73 mechanism in *P. vittata*<sup>15,17</sup>. Recently, localization of As in the apoplast near the midrib, in fronds of  
74 *P. vittata* was reported<sup>19</sup>. A similarity between the As and K distribution at both cellular and  
75 subcellular level was found<sup>15,20</sup>, implying that  $\text{K}^+$  may act as a counterbalance to  $\text{As}^{\text{V}}\text{O}_4^{3-}$  anions.

76  
77 *Pteris vittata* contains As predominantly as inorganic As species<sup>21</sup>. Regardless of whether As(III) or  
78 As(V) was supplied to the plants, the oxidized form As(V) dominated in the roots while As(III)  
79 dominated in the rhizomes and fronds<sup>15,21,22,23,24,25</sup>, suggesting that the reduction of As(V) to As(III)  
80 occurs during As translocation. Furthermore, X-ray absorption spectroscopy indicated that, in the  
81 pinnae, As(III) was predominantly coordinated with oxygen<sup>22,25</sup>. The precise location where As(V) is  
82 reduced to As(III) is still unknown. The reduction of As(V) to As(III) was firstly considered to occur  
83 in the pinnae as it was found that As in xylem sap was mainly As(V)<sup>21,23</sup>. It was proposed that As(V)  
84 is transported through the vascular tissue from the roots to the fronds, where it is reduced to As(III)  
85 and stored at high concentrations<sup>25</sup>. As(V) is reduced mainly in roots and not in the fronds<sup>22,24</sup> and  
86 root extracts from the *P. vittata* were able to reduce As(V) to As(III)<sup>26</sup>. The reduction of As mainly

87 occurs in the endodermis of roots<sup>27</sup>. Arsenic is transported in the xylem sap of *P. vittata*  
88 predominantly (93–98%) as As(III), regardless of whether As(V) or As(III) was supplied to the  
89 plants, implying that the roots are the main site of As(V) reduction in *P. vittata*<sup>29</sup>. Similar reduction  
90 of another metalloid, antimony (Sb), from pentavalent Sb to trivalent Sb has been reported in the  
91 roots of *P. vittata*<sup>30</sup>. However although clearly As(V) is reduced most effectively in root endodermis  
92 and then As(III) is transported most effectively in xylem, the identification of As(V) in other tissues  
93 means that not all of it is reduced in the root and the As(III) tris-glutathione [As(SR)<sub>3</sub>] form found in  
94 the surroundings of the vasculature suggests that reduction can occur also outside the root<sup>25</sup>.

95 Despite all the previously cited publications, no study to date has revealed the As-distribution at the  
96 cellular-scale in the *P. vittata* fronds, and previous data has only shown planar views of As  
97 (projected onto a 2D plane). As such no depth information is currently available and the *in situ* 3D  
98 distribution of As needs to be investigated and confirm the 2D visualisation. It is possible that  
99 observed differences in As speciation across tissues are due to spatial variations of As in different  
100 cell types<sup>27,31</sup>. Pickering *et al.*<sup>25</sup> examined both the gametophyte generation and the sporophyte  
101 generation, and found discrete speckles of arsenate localized in parenchymal cells (possibly in  
102 vacuoles) in the gametophytes. Another study on a related As-hyperaccumulating fern  
103 (*Pityrogramma calomelanos*) by Kachenko *et al.*<sup>7</sup> showed substantial tissue-level differentiation in  
104 As accumulation but could not reveal As chemical speciation.

105  
106 Conventional synchrotron (planar or 2D)  $\mu$ XRF of plant leaves (whole leaves or cross sections) is a  
107 projection of all elements in a sample. As such, a planar view of a plant leaf reveals the elements  
108 contained in the adaxial and abaxial epidermis and mesophyll together in a 'compressed' projected  
109 2D plane. Several methods are available for revealing the detailed 3D elemental distributions  
110 relevant to complex biological samples. In this article we employ three complementary approaches to  
111 access the 3D elemental distributions: mechanical sectioning to access the distributions within a  
112 single plane, X-ray fluorescence  $\mu$ -computed tomography (XFM- $\mu$ CT) to determine volumetric  
113 distributions from a series of projection images without sample sectioning, and confocal imaging to  
114 directly access elemental distributions within targeted regions within the specimen. Although we  
115 describe these methods here, a more detailed comparison can be found in de Jonge & Vogt<sup>32</sup> and van  
116 der Ent *et al.*<sup>33</sup>.

117  
118 Confocal optics enable a direct-space approach to deliver 3D resolution. A confocal optic confines  
119 the field of view of the energy-dispersive detector so that the signal derives from only a small portion

120 of the illuminated column<sup>34,35,36</sup>. The probe volume is thereby reduced to a spheroid and elemental  
121 distribution is mapped in three dimensions by scanning the specimen through the probe volume. The  
122 use of confocal X-ray fluorescence methods for the investigation of biological samples has been  
123 limited to date, probably due to the increased X-ray dose associated with the confocal geometry in  
124 most situations<sup>37</sup>. Such an approach was, however, successfully utilized to decipher the distribution  
125 and chemical speciation of selenium in zebrafish larvae<sup>38</sup>.

126

127 Another approach to obtain information on the internal elemental distribution in physically intact  
128 samples is X-ray fluorescence  $\mu$ -computed tomography (XFM- $\mu$ CT). This technique enables  
129 reconstruction of 2D or 3D elemental data from a rotation series of projection images. For typical  
130 measurement modalities,  $\mu$ CT requires the measurement of projection images from multiple view  
131 around a fixed rotation axis. In order to avoid issues with self-absorption and to simplify the  
132 measurement, XFM- $\mu$ CT is limited to measurements of specimen that are relatively thin in the two  
133 dimensions around the rotation axis, such as roots<sup>39,40</sup>, stems and narrow leaves<sup>41</sup> and seeds<sup>42</sup>,  
134 although  $\mu$ CT laminography could be used in flatter objects such as leaves. The confocal approach is  
135 more tolerant to self-absorption effects, and especially well-suited to measure depth profiles in  
136 extended planar objects such as leaves. Further, the confocal measurement enables direct access to  
137 small volumes within a specimen and so is amenable to direct and *in situ* spectroscopic (XANES)  
138 measurements.

139

140 Self-absorption is a combination of two effects that reduce the quantitative nature of reconstructions  
141 obtained by XFM- $\mu$ CT and affect the visualization of element distribution: the absorption of the  
142 incident X-ray photons and the re-absorption of the fluorescent X-ray photons (in particular low-  
143 energy photons) by the specimen (for a review see Vogt & de Jonge<sup>32</sup>). Self-absorption is usually  
144 dominated by the latter of these effects, and this in turn has a greater impact on the quantitative  
145 determinations of the elements with low energy x-ray photons for K-shell emission this corresponds  
146 to with lower-Z elements. Self-absorption places a practical upper limit on the specimen dimensions,  
147 so that, for example, Ni can be mapped in hydrated biological samples up to  $\sim 800$   $\mu\text{m}$  thick with  
148 reasonable accuracy ( $K\alpha$  line at 7.47 keV), but this increases up to  $\sim 1500$   $\mu\text{m}$  for As ( $K\alpha$  line at  
149 10.54 keV) assuming a tolerable limit of 50% self-absorption.

150

151 X-ray fluorescence microscopy (XFM) beamlines also offer the unique ability to perform *in situ* X-  
152 ray absorption spectroscopy (XAS) to obtain information on the chemical speciation of elements (As

153 in this case) in plant tissues without preparations and avoiding the possibility for artefacts resulting  
154 from those preparations. Moreover, the use of confocal optics allows examination of As chemical  
155 speciation at depth in distinct cell types within intact plant tissues and hence elucidation of the  
156 spatially resolved chemical speciation and elemental distribution in physically intact samples without  
157 the need for destructive sample preparation<sup>33,43</sup>.

158

159 The complexity of As distribution and chemical speciation requires a range of different  
160 methodological approaches to understand the 3D distribution at the cellular level and also for the  
161 speciation. This study uses a combination of different synchrotron X-ray methodological approaches  
162 to interrogate As distribution and chemical speciation in *Pteris vittata* tissues, which are summarised  
163 in Table 1. To date, depth-resolved information has not been available, and this study aims not only  
164 to unravel the As pathway in the As hyperaccumulating fern *Pteris vittata*, but also to demonstrate  
165 how a set of advanced synchrotron X-ray microscopy techniques can be complementary in revealing,  
166 at tissue and cellular levels, the distribution and chemical speciation of As in this hyperaccumulator  
167 plant.

168

## 169 **2. MATERIALS AND METHODS**

170

### 171 **2.1 Cultivation and collection of plant tissues and soils**

172 Tissue samples were obtained in one of two ways. Cultured tissue samples were obtained from *P.*  
173 *vittata* grown in soil at the University of Queensland. The potting mix was spiked with an As(V)  
174 solution supplied as Na<sub>2</sub>HAsO<sub>4</sub>·7H<sub>2</sub>O prior to transplanting (dose rate was 1000 mg kg<sup>-1</sup> as As). The  
175 plants were grown in a greenhouse for two months with an 11-hr daily photoperiod, a photon flux of  
176 >370 μmol m<sup>-2</sup> s<sup>-1</sup>, a day-night temperature range of 20–29°C and relative humidity of ~70%. Tissue  
177 samples of *P. vittata* were also collected from a contaminated site in Shimen, Hunan Province in  
178 south China. This site is heavily contaminated by As due to realgar ore smelting activities in the past  
179 (N29°39'33.88" E111°2'43.1") with a soil As concentration of 313 μg g<sup>-1</sup>. The live plants, together  
180 with the soil attached to the roots, were transported from Hunan to Beijing, and maintained in the  
181 laboratory in Beijing. Tissue samples intended for synchrotron XFM analysis were excised with a  
182 razor blade and immediately shock-frozen using the metal mirror freezing technique (in which the  
183 sample is rapidly pressed against a block of solid copper cooled by at -196°C liquid N<sub>2</sub>). The samples  
184 were then wrapped in Al-foil and transported in a cryogenic container (at least -190°C) for storage  
185 and transport. Samples were also freeze-dried in a freeze-dryer (LABCONCO FreeZone 6) starting at  
186 -50°C until room temperature in 48 hours. Slow freeze-drying has been shown to avoid, or at least,

187 reduce elemental re-distribution and tissue shrinkage<sup>44,45</sup> but may cause subcellular migration of  
188 dissolved elements to the nearest solid surface. The influence of freeze-drying on element chemical  
189 speciation is still contentious and depends on several factors such as the element itself, its chemical  
190 speciation and initial oxidation state<sup>46,47</sup>.

191

192 Some physical cross-sections were prepared from the cultivated *P. vittata* fronds. After shock  
193 freezing (as described earlier), the samples were cryo-transferred on dry ice (-80°C) into the cryo-  
194 chamber of the microtome (maintained at -30°C) and mounted on a plate by application of chilled (-  
195 8°C) polypropylene glycol for physical support. The fronds were then cut to 30 µm sections using a  
196 cooled blade (-20 °C), and the sections transferred to pre-cooled 1 mL cryo-containers and freeze-  
197 dried.

198

## 199 **2.2 Plant tissue bulk analysis**

200 Plant tissue samples for bulk chemical analysis were gathered from the cultured ferns after two  
201 months, and from the freeze-dried fern samples from China. The samples were dried at 70°C for five  
202 days in a dehydrating oven, subsequently ground and a 200-mg fraction digested using 4 mL  
203 concentrated nitric acid (70%) and 1 mL hydrogen peroxide (30%) in a digestion microwave oven  
204 (Milestone Start D) for a 45-minute programme. After cooling, the sample was diluted to 30 mL with  
205 TDI water. The aliquots were analysed on ICP-AES (Varian Vista Pro II) for P, Mg, Ca, K, S and  
206 As.

207

## 208 **2.3 Histochemistry and bright field microscopy**

209 Frond samples were fixed in 3% glutaraldehyde (in PBS), sectioned with a vibratome (Leica  
210 VT1000s) and stained with Toluidine Blue. The sections (20–40 µm thickness) were then examined  
211 and photographed with bright field microscope (Nikon Diskovery Spinning Disk Confocal with  
212 Andor Zyla 4.2 camera).

213

## 214 **2.4 Scanning Electron Microscopy with X-ray microanalysis (SEM-EDS)**

215 Freeze-dried leaf samples were sputter-coated with carbon (25 nm) and mounted on stubs. The  
216 samples were then imaged with Scanning Electron Microscopy (SEM) with X-ray microanalysis  
217 (Energy dispersive X ray spectroscopy or EDS) on a JEOL JSM-6610 instrument. Images were  
218 obtained for 100–1000 x magnifications at 5–15 kV with lower accelerator energies for imaging with  
219 secondary electrons only and higher accelerator energies for imaging using backscattered electrons.

220

## 221 2.5 X-ray fluorescence microscopy (XFM)

222 The X-ray fluorescence microscopy (XFM) beamline of the Australian Synchrotron employs an in-  
223 vacuum undulator to produce a brilliant X-ray beam of 4.1–20 keV with a focus down to 1000 nm. A  
224 Si(111) monochromator and a pair of Kirkpatrick-Baez (KB) mirrors deliver a monochromatic  
225 focused incident beam onto the specimen<sup>48</sup>. The P06 beamline of PETRA III (Deutsches Elektronen-  
226 Synchrotron; DESY) is also equipped with Si(111) monochromator and KB mirrors<sup>49</sup> producing X-  
227 ray beam of 5–23 keV with a focus down to 300 nm. Both beamlines are equipped with a Maia  
228 detector consisting of a large detector array to maximize the detection of fluorescence signal. The  
229 Maia detector allows for high overall count-rates and uses an annular detector geometry, where the  
230 beam passes through the detector and strikes the sample at normal incidence<sup>50,51</sup>. This geometry  
231 enables a large solid angle (1.2 steradian) to maximize detected signal and reducing the dose and  
232 potential damage to a specimen<sup>52</sup>. Maia is designed for event-mode data acquisition, where each  
233 detected X-ray event is recorded, tagged by detector number in the array, position in the scan and  
234 other metadata<sup>53</sup>. This approach eliminates readout delays and enables short pixel times (typically  
235 down to 0.1 ms) and large pixel counts to be achieved for high definition imaging (typically 10–100  
236 M pixels). The confocal experiment used a custom-made polycapillary collimating optic (XOS, input  
237 focal distance 2.5 mm, input field of view 10.0  $\mu\text{m}$ , transmission efficiency optimized for 17.4 keV  
238 radiation) fitted on a Vortex SDD detector (Hitachi Vortex EM-90, 80mm<sup>2</sup>, minimum energy of 1.6  
239 keV, energy resolution 120 eV, operated in 90-degree geometry). The experimental setup at the  
240 XFM beamline the Australian Synchrotron, showing both the Maia detector and SDD detector with  
241 confocal optic, is shown in Fig 1.

242

243 On the XFM beamline, the confocal  $\mu\text{XRF}$  and  $\mu\text{XAS}$  experiments used a polycapillary optic fitted  
244 on the SDD detector allowing for a depth resolution ( $dz$ ) of  $\sim 10 \mu\text{m}$  (energy and hence element-  
245 dependant), while the beam spot size using the KB mirrors was  $\sim 2 \mu\text{m}$ . The resolution of the  
246 polycapillary optic limits the  $z$ -resolution (along beam axis) of confocal tomography, while the beam  
247 spot size limits the  $x$ - $y$ -resolution. Accordingly, samples can be raster imaged with an effective probe  
248 volume probe of volume of  $\sim 10 \times 2 \times 2 \mu\text{m}$ . The scan was carried out in the  $x$ - $z$  plane which samples  
249 the two smallest dimension of the pinnule - a virtual section – so that the  $y$ -axis is not probed, with a  
250 1 second per pixel dwell time. The confocal  $\mu\text{-XRF}$  images were recorded using a beam incident  
251 energy of 15.8 keV

252

253 The fluorescence 2D XANES imaging at the XFM beamline was performed on a portion of a frozen-  
254 hydrated pinnule, spanning the midvein and one margin containing sporangia. The fluorescence 2D

255 XANES imaging consisted of forming ‘stacks’ of  $\mu$ XRF images by scanning the sample area  
256 multiple times at successive incident energies. As such, the sample was raster-scanned over a  $2.380$   
257  $\times$   $1.295$  mm window with a  $5$   $\mu$ m step size, resulting in a  $\mu$ -XANES image stack of  $477$   $\times$   $260$   
258 pixels. The sample was scanned over the As K-edge ( $11\ 877$  eV) at 112 energies from  $11\ 800$  to  $12$   
259  $100$  eV using  $2$  eV steps across the pre-edge region ( $11\ 800$  to  $11\ 855$  eV),  $0.5$  eV steps across the  
260 XANES region ( $11\ 855$  to  $11\ 900$  eV) and  $20$  eV across the post-edge region ( $11\ 900$  to  $12\ 100$  eV).  
261 The  $\mu$ -XANES spectra were measured using the Maia detector array with a  $\sim 1.7$  ms per pixel dwell  
262 time.

263

264 Arsenic ‘hotspots’ were identified from the confocal  $\mu$ XRF images as regions of interest for  
265 volumetric XANES point measurements. Of particular interest is the reduction of arsenate to arsenite  
266 as As species cross from the vascular system to the leaf tissues, so regions were selected in the  
267 (tissues listed in decreasing proximity to main vascular system) midvein, endodermis, mesophyll and  
268 epidermis as well as regions in the secondary veins (vein bundles and surrounding protective  
269 sheaths) and sporangia (reproductive parts of the fern). In order to obtain spatial coordination, first  
270 coarse confocal  $\mu$ XRF maps were made of the sample. Volumetric XANES point measurements  
271 were acquired using the confocal optic attached to a Vortex SDD detector (as described above) and  
272 measured across the As K-edge ( $11\ 877$  eV) at 100 energies spanning the energy range  $11\ 802$  to  
273  $12\ 017$  eV in  $0.25$  eV steps with  $0.5$ s dwell.

274

275 Energy calibration at the XFM beamline was achieved using a sample of solid sodium arsenite  
276 diluted in boron nitride. The “white line” peak energy of this sample was assumed to be  $11874.4$  eV.

277

278 The 2D  $\mu$ XRF and single-slice  $\mu$ XRF tomography measurements carried out in the microprobe of  
279 P06 at DESY were performed with a beam size of  $532$   $\times$   $444$  nm at an incident energy of  $14$  keV.  
280 Considering a minimum step size of  $0.5$   $\mu$ m and comparing it to the size of the beam, the resolution  
281 of the resulting images can be treated as being equal to the step size. Samples consisted of a free-  
282 standing rachis and two pinnule margins, one mounted between Ultralene films for 2D measurements  
283 and the other mounted inside a Kapton capillary for tomography. All scans were conducted in  
284 continuous-scanning mode to minimize dead-time between the exposures with dwell times between  $1$   
285 ms and  $10$  ms. In the case of single-slice tomography, the rotation stage was the slow scanning axis  
286 and the longer scans of the rachis were divided into eight interlaced sub-scans to account for possible  
287 vertical drift of the sample. All the samples were either freeze-dried (rachis) or dehydrated (pinnule  
288 margin) and so a cryo-stream was not employed.

289 **2.6 Sample preparation and measurement conditions**

290 All frozen-hydrated samples were scanned in using a cryo-stream, whereas the freeze-dried samples  
291 were scanned at room temperature (20°C). Individual freeze-dried pinnules were glued to carbon  
292 sticks with cyanoacrylate (Fig 1b,c), but larger samples (*i.e.* the intact ‘fresh/live’ frond) were  
293 sandwiched between two sheets of Kapton thin film (4 µm) stretched over a Perspex frame (Fig 1d)  
294 magnetically attached to the *x-y* motion stage at atmospheric temperature (~20°C). The samples were  
295 scanned ‘on-the-fly’ with a 1–5 ms per pixel dwell at an incident energy of 15.8 keV. The frozen-  
296 hydrated samples were transferred under the N<sub>2</sub> cryo-stream (-100°C) and were maintained at dry ice  
297 temperature during transfer – as such they were kept under cryogenic conditions from collection  
298 through to the completion of measurement.

299

300 **2.7 Data analysis**

301 The Maia X-ray fluorescence data were analysed using GeoPIXE<sup>54,55</sup>, and images were generated  
302 using the Dynamic Analysis method<sup>56,57</sup>. Unfortunately, due to a technical error associated with the  
303 data writing to the cluster storage the raw data of a number of 2D µXRF elemental maps were  
304 irretrievably lost. However, real-time (RT) processing data from GeoPIXE were locally retained, and  
305 the corresponding pseudo-elemental maps are included in the Supplementary Information.

306

307 Self-absorption, which can lead to inaccuracy in the determination of elemental concentration by  
308 XRM, especially in ‘thicker’ samples, depends on the composition of the material, on the thickness  
309 of the sample, on the localisation of the element to be detected and on the element itself (energy of  
310 its X-ray fluorescence lines), on the distance between sample and the detector, on the energy of the  
311 incident beam. Assuming that fern tissue has a similar composition and density to that of cellulose  
312 (C<sub>6</sub>H<sub>10</sub>O<sub>5</sub>) with an average thickness of 300 µm (a pinnule blade is somewhat thinner at ~80 µm  
313 whereas a rachis is thicker at ~500 µm) and a density of 1.0 g cm<sup>-3</sup> then it is assumed that the As  
314 fluorescence (K<sub>alpha</sub> line at 10.5 KeV) maximum absorption on escape is ~10%.

315

316 Confocal XRF imaging data were analysed with MAPS. Because the (element-dependant)  
317 transmission efficiency of the polycapillary optic is not known, and because of the different  
318 geometric orientations of the sample (resulting in varying X-ray flux on the sample), the confocal  
319 elemental maps were not quantified with respect to concentrations of particular elements. The  
320 concentrations are hence plotted on a relative scale.

321

322 Analysis of the XFM- $\mu$ CT data was achieved by alignment steps using consistency and cross-  
323 correlation methods to correct for horizontal drift in the sinograms followed by a tomographic  
324 reconstruction step. The high angular sampling of the rachis allowed reconstruction using a filtered  
325 back-projection algorithm. However, the pinnule sinograms were recorded with lower angular  
326 sampling and so were reconstructed with a maximum-likelihood expectation-maximization algorithm  
327 based on the functions of the *scikit-image* image processing library.

328

329 Fluorescence-XANES mapping gave a 3D image stack of spatial dimensions ( $x, y$ ) and an X-ray  
330 incident energy-resolved dimension  $E$ . Initially, the XANES images were aligned using a well-  
331 featured spectator element. Alternatively, one could consider each pixel ( $x, y$ ) of the  $477 \times 260$ -pixel  
332 image stack to be associated with a unique XANES spectrum. The energy variation in the  
333 fluorescence spectra were identified using principal component analysis (PCA) allowing for up to six  
334 principal components, with the calculations performed using the Multivariate ANalysis Tool for  
335 Spectromicroscopy (MANTiS, Lerotic). Pixels possessing similar spectra were grouped together by  
336  $k$ -means clustering, identifying three distinct clusters associated with the leaf, vein and image  
337 background (Figure 10). The cluster associated with the background of the image has been  
338 subtracted from composite image in Figure 10.

339

### 340 **3. RESULTS.**

341

#### 342 **3.1 Bulk chemistry and anatomical features**

343 Although *P. vittata* can reach up to  $22\,600\ \mu\text{g g}^{-1}$  As dry weight in its fronds<sup>4</sup>, the cultured plants  
344 display  $1354\ \mu\text{g g}^{-1}$  and field collected plants from China have  $8580\ \mu\text{g g}^{-1}$  As on a dry weight basis  
345 (Table 2). The concentration of Ca is relatively high in the pinnae with up to  $10\,300\ \mu\text{g g}^{-1}$ , whereas  
346 the K concentration is extremely high in both the pinnae and rachis ranging from  $12\,300$  to  $33\,000$   
347  $\mu\text{g g}^{-1}$ . The concentration of P is exceptionally high, especially in the samples from China with up to  
348  $62\,700\ \mu\text{g g}^{-1}$  in the pinnae and up to  $67\,000\ \mu\text{g g}^{-1}$  in the rachis. Concentrations of Cu, Zn and Fe are  
349 unremarkable. Toluidine blue stained *P. vittata* sections of the rachis (Fig. 2) show the typical  
350 anatomy of a pteridophyte with the C-shaped elliptical vascular bundles surrounded by three-cell  
351 thick pericycle and endodermis cells. The mesophyll is not differentiated into palisade and spongy  
352 parenchyma, and mesophyll is absent from the mid-rib. Scanning Electron Microscopy (SEM)  
353 images show details of the sporangium with sporophytes (Fig. 3). Each sorus contains clusters of  
354 sporangia protected by the upper indusial flap ('false indusium') that is formed by the margins of the

355 pinnule. The abundant presence of fertile cells is evident with the sporangium showing individual  
356 sori enclosed by large annulus cells.

357

### 358 **3.2 Planar elemental imaging, confocal ‘virtual’ and computed tomography slices**

359 The 2D projection  $\mu$ XRF elemental maps of the live frond (Fig. 4) show substantial enrichment of  
360 As in the vascular bundles, particularly in the rachis, but also in the veins of the pinnule. There is a  
361 depletion of As in the interveinal areas of the pinnule. The localisation of K is similar except that its  
362 concentration in the rachis is higher than the mean As concentration in fronds. In contrast, Ca is  
363 depleted in the rachis, but enriched in the veins of the pinnule particularly towards the terminal ends.  
364 Calcium is also enriched in damaged (chlorotic) parts of the fronds, mainly along the margins. These  
365 differences are more pronounced in the high-resolution scans of the pinnule apex (Fig. 5), with Ca  
366 depleted in the veins but enriched along the pinnule margins. The distribution of As and K are again  
367 similar although the distribution of K extends into the lamina. In the freeze-dried pinnule portion  
368 towards the terminus (Suppl. Fig. S1 A, B), the distribution of As mirrors that of the frozen-hydrated  
369 samples with substantial enrichment in the vascular bundles, especially in the central vein. In fertile  
370 pinnules (Suppl. Fig. 1, C, D) strong accumulation of As in the sorus and sporangia is visible.  
371 Further detail can be gleaned from scans of the sori (Suppl. Fig. 2). Apart from As enriched in the  
372 indusium, the strongest accumulation occurs in the annulus of each sporangium. Some of the  
373 individual spores are also rich in As (see top-right panel, Fig. 9), as are hairs in the sorus (for  
374 example bottom right panel Fig. 9). Enrichment in the hairs that guard the sporangium at the margin  
375 of the fronds has been noted previously<sup>25</sup>.

376

377 Higher resolution 2D  $\mu$ XRF images (up to 0.5  $\mu$ m) were collected of the (freeze-dried) pinna margin  
378 containing the indusium covering the sporangia, which reveals that As is enriched predominantly in  
379 the vascular bundles connecting to the sporangia, but little in the sori themselves (Suppl. Figs. 6, 7,  
380 and 8). K is enriched along the indusium edge, and Zn highly localised in the mature sori.  
381 Fluorescence computed  $\mu$ -tomography slices and projections of an intact pinna (Fig. 8 and 9, 0.5  $\mu$ m  
382 pixels) similarly reveal As enrichment in the vascular structures, especially in nodes, but also in  
383 some sori.

384

385 Elemental maps of As, Br, Ca and Rb obtained from confocal ‘virtual’ cross-sections of a pinnule are  
386 shown in Suppl. Fig. 9. The self-absorption effect as a function of element  $z$  is clearly visible from  
387 the Ca elemental map with a ‘shadow’ evident behind the thicker midrib. For that reason, we have  
388 plotted maps of (high  $Z$ ) Rb and Br to serve as proxies for K and Cl respectively. The elemental

389 distribution of Rb is similar to As, which was expected on the basis of the earlier observed  
390 similarities between As and K. Arsenic is localised in the adaxial (upper) epidermis extending into  
391 the palisade mesophyll. Arsenic is also strongly enriched in the phloem of the (sub)lateral veins.  
392 Confocal cross-sections of the central part of the pinnule with the midrib reveal that As is strongly  
393 accumulated in the endodermis and pericycle surrounding the phloem (Fig. 6). Arsenic is also  
394 strongly enriched in abaxial (lower) epidermal cells of the midrib (but not extending to the lamina).  
395 Detailed confocal scans of the pinnule margins show accumulation of As in the indusium as well as  
396 in the sporangia, particularly the annulus (Suppl. Fig 10).

397

398 The elemental distribution of As in freeze-dried physical cross-sections scanned in 2D (Suppl. Fig.  
399 3–4) also shows strong enrichment in the endodermis and pericycle surrounding the vascular  
400 bundles, as well as in the hypodermis extending into the cortex, ostensibly in the apoplastic space  
401 between the cells. Again, As is accumulated in the indusium and in the annulus of the sporangia. A  
402 scan of a physically sectioned freeze-dried rachis (Suppl. Fig. 5) shows the accumulation of As in the  
403 endodermis and pericycle surrounding the phloem. Fluorescence computed  $\mu$ -tomography with 0.5  
404  $\mu\text{m}$  pixel size was undertaken on a freeze-dried rachis (Fig. 7) and reveals a very similar As  
405 enrichment pattern in the endodermis and pericycle surrounding the vascular bundles.

406

### 407 **3.3 XANES imaging and volumetric XANES spot analysis**

408 2D XANES imaging was performed on a frozen-hydrated pinnule. In addition, volumetric XANES  
409 measurements were acquired from spatial regions of interest in pinnae in both freeze-dried samples  
410 recorded at room temperature (Suppl. Figs. 11 and 12) and frozen-hydrated state under a cryostream  
411 using a confocal optic.

412

413 The cluster spectra associated with the pinnule and vascular bundle areas respectively were  
414 compared to reference spectra of relevant As standards (figure 10C). On the basis of the energy  
415 position of the absorption maxima, and comparison to the spectrum of solid sodium arsenite recorded  
416 during the same beamtime run, cluster 1 and 2 spectra were assumed to correspond to As(III) (as  
417 arsenite) and As(V) (as arsenate), respectively. Both spectra are slightly broadened in comparison  
418 with reference spectra reproduced from previous study<sup>25</sup> that were recorded with higher energy  
419 resolution (0.2 instead of 0.5 eV). However, the spectrum extracted from cluster 2 in Fig 10,  
420 primarily representing the main vascular bundle zone, displays an even broader absorption edge,  
421 displaying a shoulder at lower energy consistent with the peak energy of the arsenite model

422 spectrum. This broadening is likely due to the presence of a mixture of As(III) and (V) species in the  
423 vascular bundles, where the relative abundance of each species is consistent across the cluster.

424

425 Volumetric XANES point measurements from a selection of different anatomical features returned  
426 spectra that were distinct from the model compound spectra. Absorption peak energies were aligned  
427 more closely to those of the As(III) standards, even in tissues where As(V) would be expected from  
428 previous work and from the 2D XANES imaging in this work (Figure 10). For instance, it is  
429 expected that the vascular bundles (regions G and H, Suppl Fig. 11) would exhibit As(V) prior to  
430 crossing the endodermis, however these bundles display reduced As(III) as stated from the peak  
431 energy. The peak height to background edge jump ratio in several of the volumetric XANES spectra  
432 is drastically attenuated relative to the model spectra. The results of the volumetric XANES analysis  
433 suggest that this approach delivers too high of a radiation dose to the sample to be reliable in  
434 determining the speciation of As in the specimen without drastic photoreduction, even in samples  
435 cooled under a liquid N<sub>2</sub> cryostream. In fact, point XANES spectra from freeze-dried tissues (Suppl  
436 Fig 12), which should be less susceptible to photoreduction due to the absence of water, show higher  
437 peak energies in some cases compared to those spectra from frozen tissue, strongly implicating  
438 photodamage in the unusual appearance of these spectra.

439

440 The XANES spectra collected using either 2D XANES imaging or confocal point XANES are  
441 compared below to model As compound spectra previously reported<sup>25</sup>. We note that the spectral  
442 resolution of the beamline used in this work is significantly poorer than that from the previous work;  
443 as such, any comparison should be interpreted with caution as the spectra from this study will be  
444 broadened significantly compared to the model compound spectra.

445

#### 446 **4. DISCUSSION**

447 The use of confocal optics has made it possible to examine As in the depth profile of the tissues in  
448 physically intact samples with high aspect ratio, without the need for destructive sample preparation,  
449 and this approach has provided new information on the mechanisms underlying As  
450 hyperaccumulation in *P. vittata*. Confocal cross-sections of the central part of the pinnule with the  
451 midrib have revealed that As is strongly accumulated in the endodermis and pericycle surrounding  
452 the phloem. XFM  $\mu$ -CT revealed a very similar As enrichment pattern in the endodermis and  
453 pericycle surrounding the vascular bundles. As such, the various technical approaches lead to  
454 conclusions that are entirely consistent with each other.

455

456 Confocal optics also offer the ability to perform volumetric XANES to obtain spatially resolved  
457 information on the chemical speciation within intact tissues. However, it eventuated that volumetric  
458 XANES causes substantial photodamage due to the very high radiation dose of this approach (60s  
459 total exposure per point), even if the sample is cryogenically cooled. Therefore, observations indicate  
460 that significant interpretation regarding As chemical form should not be drawn from the confocal  
461 volumetric XANES measurements, and reiterate the utility of 2D XANES imaging to provide  
462 chemical information with lower X-ray dose (0.0017s total exposure per pixel, or ~300 less than then  
463 confocal XANES measurements), albeit without the capacity to provide information in the third  
464 dimension in this case. The results of the 2D XANES imaging are congruent with previous  
465 knowledge of As speciation in *P. vittata*<sup>25</sup>, which in part validates the novel confocal imaging in this  
466 work as it demonstrates that the sample preparation has not modified the distribution of the primary  
467 arsenic species in the tissues. Published 2D XANES imaging studies showed that different chemical  
468 forms of As (As(III) and As(V)) occur across the plant organs<sup>25</sup>. Depth information of As chemical  
469 speciation in different cell types within tissues of *P. vittata* was not available and the knowledge of  
470 the distribution across different cells types within the fronds and rachis was limited<sup>28</sup>. In this work  
471 we have demonstrated that observed differences in As speciation across tissues are related to spatial  
472 variation of As concentration in different cell types.

473

474 After the Zn-Ni-Cd hyperaccumulator *Noccaea caerulescens*, *P. vittata* is the most well-studied  
475 hyperaccumulator. As a consequence, much is now known about the uptake and metabolic regulation  
476 of As in this species<sup>19,21,22,26,25,28,31,30</sup>. Nevertheless, many open questions remain, specifically  
477 surrounding the adaptive advantages for As hyperaccumulation in this species, and about the  
478 physiological functions of As(V) to As(III) conversion for storage and translocation in the fronds.

479

#### 480 **Author contributions**

481 M.L and X-M.W collected the *P. vittata* samples in the field in China. A.vdE cultivated live *P.*  
482 *vittata* in Australia. X-M.W prepared freeze-dried samples for the synchrotron analysis. A.vdE,  
483 M.dJ, E.M-P, G.E. and H.H.H conducted the synchrotron XFM experiments. M.dJ, R.MP and H.H.H  
484 analysed the XFM and XAS data. A.vdE performed the SEM-EDS and light microscopy  
485 experiments. A.vdE, K.M.S and D.B performed the synchrotron  $\mu$ XRF tomography experiments.  
486 K.M.S analysed the  $\mu$ XRF tomography spectra. D.B reconstructed the  $\mu$ XRF tomograms. All authors  
487 contributed to writing the manuscript.

488

489

490 **Acknowledgements**

491 This research was undertaken on the X-Ray Fluorescence Microscopy beamline of the Australian  
492 Synchrotron (part of ANSTO), Victoria, Australia. This work was supported by the Multi-modal  
493 Australian ScienceS Imaging and Visualisation Environment (MASSIVE). Beamtime at beamline  
494 P06 at PETRA III was granted within the in-house research program of DESY, a member of the  
495 Helmholtz-Association. We would like to thank Jan Garrevoet for assistance during the experiments.  
496 We thank the Centre for Microscopy and Microanalysis, The University of Queensland. A. van der  
497 Ent was the recipient of a Discovery Early Career Researcher Award (DE160100429) from the  
498 Australian Research Council. H. Harris acknowledges the Australian Research Council for financial  
499 support (DP140100176). The French National Research Agency through the national  
500 “Investissements d’avenir” program (ANR-10-LABX-21, LABEX RESSOURCES21) and through  
501 the ANR-14-CE04-0005 Project “Agromine” is acknowledged for funding support to A. van der Ent.  
502 Finally, the Program “Bingwei” Excellent Talent in the Institute of Geographic Sciences and Natural  
503 Resources Research, CAS supported this work.

504

505 **REFERENCES**

506

507 1 Krämer U. 2010. Metal Hyperaccumulation in Plants. *Annu. Rev. Plant Biol.* 61: 517–534.

508

509 2 Pollard AJ, Powell KD, Harper FA, Smith JAC. 2002. The Genetic Basis of Metal  
510 Hyperaccumulation in Plants. *Critical Reviews in Plant Sciences* 21: 539–566.

511

512 3 Reeves RD, Baker AJM, Jaffré T, Erskine PD, Echevarria G, van der Ent A. 2017. A global  
513 database for hyperaccumulator plants of metal and metalloid trace elements. *New Phytologist* 18:  
514 407–411.

515

516 4 Ma LQ, Komar KM, Tu C, Zhang WH, Cai Y, Kennelley ED. 2001. A fern that hyperaccumulates  
517 arsenic. *Nature* 411(6836): 438-U3.

518

519 5 Tu C, Ma LQ. 2003. Effects of arsenate and phosphate on their accumulation by an arsenic-  
520 hyperaccumulator *Pteris vittata* L. *Plant and Soil* 249: 373–382.

521

- 522 6 Francesconi K, Visoottiviseth P, Sridokchan W, Goessler W. 2002. Arsenic species in an arsenic  
523 hyperaccumulating fern, *Pityrogramma calomelanos*: a potential phytoremediator of arsenic-  
524 contaminated soils. *Science of the Total Environment*, The 284: 27–35.
- 525
- 526 7 Kachenko AG, Bhatia NP, Singh B, Siegele R. 2007. Arsenic hyperaccumulation and localization  
527 in the pinnule and stipe tissues of the gold-dust fern (*Pityrogramma calomelanos* (L.) Link var.  
528 *austroamericana* (Domin) Farw.) using quantitative micro-PIXE spectroscopy. *Plant and Soil* 300:  
529 207–219.
- 530
- 531 8 Chen, T., Li, H., Lei, M., Wu, B., Song, B., Zhang, X., 2010. Accumulation of N, P and K  
532 in *Pteris vittata* L. during phytoremediation: a five-year field study. *Acta Sci.*  
533 *Circumstantiae* 30, 402e408.
- 534
- 535 9 Xie Q-E, Yan X-L, Liao X-Y, Li X. 2009. The Arsenic Hyperaccumulator Fern *Pteris vittata* L.  
536 *Environmental Science & Technology* 43: 8488–8495.
- 537
- 538 10 Iriel, A., Lagorio, M.G., Cirelli, A.F., 2015. Biosorption of arsenic from groundwater using  
539 *Vallisneria gigantea* plants. Kinetics, equilibrium and photophysical considerations. *Chemosphere*  
540 138, 383e389.
- 541
- 542 11 Vetterlein, D., Wesenberg, D., Nathan, P., Bräutigam, A., Schierhorn, A., Mattusch, J., Jahn, R.,  
543 2009. *Pteris vittata* Revisited: Uptake of As and its speciation; impact of P, role of phytochelatins and  
544 S. *Environ. Pollut.* 157, 3016-3023
- 545
- 546 12 Poynton CY, Huang JW, Blaylock MJ, Kochian LV, Elless MP. 2004. Mechanisms of arsenic  
547 hyperaccumulation in *Pteris* species: root As influx and translocation. *Planta* 219: 1080–1088.
- 548
- 549 13 Danh LT, Truong P, Mammucari R, Foster N. 2013. A Critical Review of the Arsenic Uptake  
550 Mechanisms and Phytoremediation Potential of *Pteris vittata*. *International Journal of*  
551 *Phytoremediation* 16: 429–453.
- 552
- 553 14 Li JT, Gurilian K, Wu LH, van der Ent A, Qiu RL, Baker AJM, Tang YT, Yang X, Shu WS.  
554 2018. Arsenic, cadmium, copper, manganese, REE, selenium and zinc hyperaccumulator plants from

555 China: a synthesis on the current state of knowledge. *Environmental Science & Technology* 52, 21:  
556 11980-11994.

557

558 15 Lombi E, Zhao FJ, Fuhrmann M, Ma LQ. 2002. Arsenic distribution and speciation in the fronds  
559 of the hyperaccumulator *Pteris vittata*. *New Phytologist* 156: 195–203.

560

561 16 Chen TB, Huang ZC, Huang YY, Lei M. 2005. Distributions of arsenic and essential elements in  
562 pinnule of arsenic hyperaccumulator *Pteris vittata* L. *Science in China Series C-Life Sciences* 48(1):  
563 18-24.

564

565 17 Li WX, Chen TB, Chen Y, Lei M. 2005. Role of trichome of *Pteris vittata* L. in arsenic  
566 hyperaccumulation. *Science in China Series C-Life Sciences* 48(2): 148–154.

567

568 18 Chen TB, Yan XL, Liao XY, Xiao XY, Huang ZC, Xie H, Zhai LM. 2005. Subcellular  
569 distribution and compartmentalization of arsenic in *Pteris vittata* L. *Chinese Science Bulletin* 50(24):  
570 2843–2849.

571

572 19 Datta R, Das P, Tappero R, Punamiya P, Elzinga E, Sahi S, Feng H, Kiiskila J, Sarkar D. 2017.  
573 Evidence for exocellular Arsenic in Fronds of *Pteris vittata*. *Scientific Reports* 7: 579–8.

574

575 20 Huang ZC, Chen TB, Lei M, Liu YR, Hu TD. 2008. Difference of Toxicity and Accumulation of  
576 Methylated and Inorganic Arsenic in Arsenic-Hyperaccumulating and -Hypertolerant Plants.  
577 *Environmental Science & Technology* 42(14): 5106–5111.

578

579 21 Zhang, W. H.; Cai, Y.; Tu, C.; Ma, L. Q, 2002. Arsenic speciation and distribution in an arsenic  
580 hyperaccumulating plant. *Science of the Total Environment* 300(1-3): 167–177.

581

582 22 Huang ZC, Chen TB, Lei M, Hu TD. 2004. Direct determination of arsenic species in arsenic  
583 hyperaccumulator *Pteris vittata* by EXAFS. *Acta Botanica Sinica* 46(1): 46–50.

584

585 23 Kertulis GM, Ma, LQ, MacDonald GE, Chen R, Chen R, Winefordner JD, Cai Y. 2005. Arsenic  
586 speciation and transport in *Pteris vittata* L. and the effects on phosphorus in the xylem sap.  
587 *Environmental and Experimental Botany* 54 (3): 239–247.

588

589 24 Mathews S, Ma LQ, Rathinasabapathi B, Natarajan S, Saha UK. 2010. Arsenic transformation in  
590 the growth media and biomass of hyperaccumulator *Pteris vittata* L. *Bioresource Technology*  
591 101(21): 8024–8030.  
592

593 25 Pickering IJ, Gumaelius L, Harris HH, Prince RC, Hirsch G, Banks JA, Salt DE, George GN.  
594 2006. Localizing the Biochemical Transformations of Arsenate in a Hyperaccumulating Fern.  
595 *Environmental Science & Technology* 40: 5010–5014.  
596

597 26 Duan GL, Zhu YG, Tong YP, Cai C, Kneer R. 2005. Characterization of arsenate reductase in the  
598 extract of roots and fronds of Chinese brake fern, an arsenic hyperaccumulator. *Plant Physiology*  
599 138(1): 461–469.  
600

601 27 Lei M, Wan XM, Huang ZC, Chen, TB, Li, XW, Liu YR. 2012. First evidence on different  
602 transportation modes of arsenic and phosphorus in arsenic hyperaccumulator *Pteris vittata*.  
603 *Environmental Pollution* 161: 1–7.  
604

605 28 Wan X, Lei M, Chen T, Ma J. 2017. Micro-distribution of arsenic species in tissues of  
606 hyperaccumulator *Pteris vittata* L. *Chemosphere* 166: 389–399.  
607

608 29 Su YH, McGrath SP, Zhu YG, Zhao FJ. 2008. Highly efficient xylem transport of arsenite in the  
609 arsenic hyperaccumulator *Pteris vittata*. *New Phytologist* 180: 434–441.  
610

611 30 Wan X, Lei M, Chen TB. 2016. Interaction of As and Sb in the hyperaccumulator *Pteris vittata*  
612 L.: changes in As and Sb speciation by XANES. *Environmental Science and Pollution Research*: 1–  
613 9.  
614

615 31 Caille N, Zhao FJ, McGrath SP. 2004. Comparison of root absorption, translocation and tolerance  
616 of arsenic in the hyperaccumulator *Pteris vittata* and the nonhyperaccumulator *Pteris tremula*. *New*  
617 *Phytologist* 165: 755–761.  
618

619 32 de Jonge MD, Vogt S. 2010. Hard X-ray fluorescence tomography-an emerging tool for structural  
620 visualization. *Current Opinion in Structural Biology* 20: 606–614.  
621

622 33 van der Ent A, Przybyłowicz WJ, de Jonge MD, Harris HH, Ryan CG, Tylko G, Paterson DJ,  
623 Barnabas AD, Kopittke PM, Mesjasz-Przybyłowicz J. 2017. X-ray elemental mapping techniques for  
624 elucidating the ecophysiology of hyperaccumulator plants. *New Phytologist* 218: 432–452.  
625

626 34 Kanngiesser B, Malzer W, Reiche I. 2003. A new 3D micro X-ray fluorescence setup — first  
627 archaeometric applications. *Nuclear Instruments and Methods in Physics Research Section B* 211:  
628 259–264.  
629

630 35 Janssens K, Proost K, Falkenberg G. 2004. Confocal microscopic X-ray fluorescence at the  
631 Hasylab microfocus beamline: characteristics and possibilities. *Spectrochimica Acta Part B* 59(533):  
632 1637–1645.  
633

634 36 Vincze L, Vekemans B, Brenker FE, Falkenberg G, Rickers K, Somogyi, Kersten SM, Adams F.  
635 2004. Three dimensional trace element analysis by confocal X-ray microfluorescence imaging.  
636 *Analytical Chemistry* 76: 6786–6791.  
637

638 37 Chukalina M, Simionovici A, Zaitsev S, Vanegas CJ. 2007. Quantitative comparison of X-ray  
639 fluorescence microtomography setups: Standard and confocal collimator apparatus. *Spectrochimica*  
640 *Acta Part B: Atomic Spectroscopy* 62: 544–548.  
641

642 38 Choudhury S, Thomas JK, Sylvain NJ, Ponomarenko O, Gordon RA, Heald SM, Janz DM, Krone  
643 PH, Coulthard I, George GN, Pickering IJ. 2015. Selenium Preferentially Accumulates in the Eye  
644 Lens Following Embryonic Exposure: A Confocal X-ray Fluorescence Imaging Study.  
645 *Environmental Science & Technology* 49: 2255–2261.  
646

647 39 Kopittke PM, Menzies NW, de Jonge MD, McKenna BA, Donner E, Webb RI, Paterson DJ,  
648 Howard DL, Ryan CG, Glover CJ, Scheckel KG, Lombi E. 2011. In Situ Distribution and Speciation  
649 of Toxic Copper, Nickel, and Zinc in Hydrated Roots of Cowpea. *Plant Physiology* 156: 663–673.  
650

651 40 Lombi E, de Jonge MD, Donner E, Kopittke PM, Howard DL, Kirkham R, Ryan CG, Paterson D.  
652 2011. Fast X-Ray Fluorescence Microtomography of Hydrated Biological Samples (JM Schnur,  
653 Ed.). *PLoS ONE* 6: e20626–5.  
654

655 41 McNear DH Jr, Peltier E, Everhart J, Chaney RL, Sutton S, Newville M, Rivers M, Sparks DL.  
656 2005. Application of quantitative fluorescence and absorption-edge computed microtomography to  
657 image metal compartmentalization in *Alyssum murale*. *Environmental Science & Technology* 39:  
658 2210–2218.

659

660 42 Kim SA, Punshon T, Lanzirotti A, Li L, Alonso JM. 2006. Localization of iron in *Arabidopsis*  
661 seed requires the vacuolar membrane transporter VIT1. *Science* 314: 1295–1298.

662

663 43 Kopittke PM, Punshon T, Paterson DJ, Tappero RV, Wang P, Blamey FPC, van der Ent A,  
664 Lombi E. 2018. Synchrotron-Based X-Ray Fluorescence Microscopy as a Technique for Imaging of  
665 Elements in Plants. *Plant Physiology* 178: 507–523.

666

667 44 Tylko G, Mesjasz-Przybyłowicz J and Przybyłowicz WJ. 2007. X-ray microanalysis of biological  
668 material in the frozen-hydrated state by PIXE. *Microscopy Research and Technique* 70: 55–68.

669

670 45 Wang YD, Mesjasz-Przybyłowicz J, Tylko G, Barnabas AD, Przybyłowicz WJ. 2013. Micro-  
671 PIXE analyses of frozen-hydrated semi-thick biological sections *Nuclear Instruments and Methods*  
672 *in Physics Research Section B: Beam Interactions with Materials and Atoms* 306: 134–139.

673

674 46 George GN, Pickering IJ, Pushie MJ, Nienaber K, Hackett MJ, Ascone I, Hedman B, Hodgson  
675 KO, Aitken JB, Levina A, Glover C, Lay PA. 2012. X-ray-induced photo-chemistry and X-ray  
676 absorption spectroscopy of biological samples. *Journal of Synchrotron Radiation* 19: 875–886.

677

678 47 Wang P, McKenna BA, Menzies NW, Li C, Glover CJ, Zhao F-J, Kopittke PM. 2019.  
679 Minimizing experimental artefacts in synchrotron based X-ray analyses of Fe speciation in plant  
680 tissues of rice plants. *Journal of Synchrotron Radiation* 26. DOI: 10.1107/S1600577519004351

681

682 48 Paterson DJ, De Jonge MD, Howard DL, McKinlay WLJ, Starritt A, Kusel M, Ryan CG,  
683 Kirkham R, Moorhead G, Siddons DP. 2011. The x-ray fluorescence microscopy beamline at the  
684 Australian synchrotron. *AIP Conf. Proc.* 1365, 219.

685

686 49 Schroeder W, De Samber B. 2014. A Cryogenic Sample Environment for the Analysis of Frozen  
687 Hydrated Biological Tissue at the Hard X-ray Micro/Nano-Probe Beamline P06 at PETRA III.  
688 *Photon Science*.

689 50 Kirkham R, Dunn PA, Kuczewski A, Siddons DP, Dodanwela R, Moorhead GF, Ryan CG, De  
690 Geronimo G, Beuttenmuller R, Pinelli D, Pfeffer M, Davey P, Jensen M, Paterson D, de Jonge MD,  
691 Kusel M and McKinlay J, 2010, The Maia Spectroscopy Detector System: Engineering for  
692 Integrated Pulse Capture, Low-Latency Scanning and Real-Time Processing, *AIP Conference series*  
693 1234: 240–243.

694

695 51 Siddons DP, Kirkham R, Ryan CG, De Geronimo G, Dragone A, Kuczewski AJ, Li ZY, Carini  
696 GA, Pinelli D, Beuttenmuller R, Elliott D, Pfeffer M, Tyson TA, Moorhead GF, Dunn PA 2014.  
697 Maia X-ray Microprobe Detector Array System. *Journal of Physics: Conference Series* 499:  
698 012001–10.

699

700 52 Ryan CG, Kirkham R, Hough RM, Moorhead G, Siddons DP, de Jonge MD, Paterson DJ, De  
701 Geronimo G, Howard DL, Cleverley JS. 2010. Elemental X-ray imaging using the Maia detector  
702 array: The benefits and challenges of large solid-angle. *Nuclear Instruments and Methods in Physics*  
703 *Research Section A: Accelerators, Spectrometers, Detectors and Associated Equipment* 619: 37–43.

704

705 53 Ryan CG, Siddons DP, Kirkham R, Li ZY, de Jonge MD, Paterson DJ, Kuczewski A, Howard  
706 DL, Dunn PA, Falkenberg G, Boesenberg U, De Geronimo G, Fisher LA, Halfpenny A, Lintern MJ,  
707 Lombi E, Dyl KA, Jensen M, Moorhead GF, Cleverley JS, Hough RM, Godel B, Barnes SJ, James  
708 SA, Spiers KM, Alfeld M, Wellenreuther G, Vukmanovic Z, Borg S. 2014. Maia X-ray fluorescence  
709 imaging: Capturing detail in complex natural samples. *Journal of Physics: Conference Series* 499:  
710 012002–12.

711

712 54 Ryan CG, Cousens DR, Sie SH, Griffin WL. 1990. Quantitative analysis of PIXE spectra in  
713 geoscience applications. *Nuclear Instruments and Methods in Physics Research Section B: Beam*  
714 *Interactions with Materials and Atoms* 49: 271–276.

715

716 55 C.G. Ryan, B.E. Etschmann, S. Vogt, J. Maser, C.L. Harland, E. van Achterbergh and D. Legnini,  
717 (2005), "Nuclear Microprobe – Synchrotron Synergy: Towards Integrated Quantitative Real-time  
718 Elemental Imaging using PIXE and SXRF", *Nucl. Instr. Meth. B*231, 183-188.

719

720 56 Ryan CG, Jamieson DN. 1993. Dynamic analysis: on-line quantitative PIXE microanalysis and its  
721 use in overlap-resolved elemental mapping. *Nuclear Instruments and Methods in Physics Research*  
722 *Section B: Beam Interactions with Materials and Atoms* 77: 203–214.

723 57 Ryan CG. 2000. Quantitative trace element imaging using PIXE and the nuclear microprobe.  
724 *International Journal of Imaging Systems and Technology* 11(4): 219–230.  
725

726 **FIGURE CAPTIONS**

727

728 **Figure 1.** Experimental setup at the XFM beamline of the Australian Synchrotron: **[A]** Schematic  
729 diagram of confocal probe, SDD – silicon drift detector (image by Gary Ruben) **[B]** frozen-hydrated  
730 sample under the cryo-stream in front of the Maia detector; **[C]** Frozen-hydrated samples probed  
731 with the confocal optic; **[D]** Maia planar imaging at room temperature of a large live frond still  
732 attached to the plant (with rhizome in pouch with moist cotton). Typical dimensions of the probe  
733 beam are  $\sim 1 \mu\text{m}$ , those of the confocal field of view are  $\sim 10 \mu\text{m}$ , and the specimen thickness is in the  
734  $>100 \mu\text{m}$  domain.

735

736 **Figure 2.** Toluidine blue stained *Pteris vittata* sections: **[clockwise from top left]** section of the  
737 rachis; section of the central part of the frond; unstained and stained sections of the sporophytes  
738 attached to the frond. Abbreviations: *LE* lower epidermis, *UE* upper epidermis, *C* cortex, *P* pamenta,  
739 *VB* vascular bundle, *Ct* cuticle, *H* hypodermis, *M* mesophyll, *X* xylem, *E* endodermis, *Pe* pericycle,  
740 *Ph* phloem, *R* receptacle, *I* false indusium, *Ha* hair, *Ys* young sporangium, *Ms* mature sporangium, *A*  
741 annulus, *S* stomium.

742

743 **Figure 3.** Scanning Electron Microscopy (SEM) images of *Pteris vittata* tissues: **[A]** sporangium  
744 enclosures within the margin of the frond (indusium); **[B]** detail of sporophytes showing **[C]** vascular  
745 bundles of the rachis; **[D]** detail of central xylem bundles.

746

747 **Figure 4.** Planar  $\mu\text{XRF}$  maps of Ca, K and As of a live *Pteris vittata* frond examined at room  
748 temperature. Relative concentrations are depicted by shading with brighter colours equating to higher  
749 concentrations ('heatmap').

750

751 **Figure 5.** Planar  $\mu\text{XRF}$  maps of Ca, K, As and Compton Scatter of the terminal ends of a live *Pteris*  
752 *vittata* frond examined at room temperature. Relative concentrations are depicted by shading with  
753 brighter colours equating to higher concentrations ('heatmap').

754

755 **Figure 6.** Confocal  $\mu\text{XRF}$  virtual section elemental maps of As in *Pteris vittata* fronds (central  
756 part/rachis). Panels: **[A]** freeze-dried f examined at room temperature; **[B]** frozen-hydrated examined  
757 under the cryostream; **[C]** freeze-dried f examined at room temperature; **[D]** frozen-hydrated  
758 examined under the cryostream. Relative concentrations are depicted by shading with brighter  
759 colours equating to higher concentrations ('heatmap').

760 **Figure 7** Single-slice  $\mu$ XRF tomogram of a freeze-dried *Pteris vittata* rachis examined at room  
761 temperature showing As and Compton signals. Relative concentrations are depicted by shading with  
762 brighter colours equating to higher concentrations ('heatmap').

763

764 **Figure 8.** Single-slice  $\mu$ XRF tomograms of a freeze-dried *Pteris vittata* pinnule margin inside a  
765 Kapton capillary examined at room temperature showing As and Compton signals. Relative  
766 concentrations are depicted by shading with brighter colours equating to higher concentrations  
767 ('heatmap').

768

769 **Figure 9.** 2D  $\mu$ XRF maps of a freeze-dried *Pteris vittata* pinnule margin inside a Kapton capillary  
770 examined at room temperature showing As and Compton signals from different angles. Relative  
771 concentrations are depicted by shading with brighter colours equating to higher concentrations  
772 ('heatmap').

773

774 **Figure 10.** *Left:* As elemental map of a portion of *Pteris vittata* pinnule including midvein and leaf  
775 margin, taken at the top energy of the 2D XANES imaging scan (12.1 keV). *Middle:* composite of  
776 cluster maps generated by  $k$ -means clustering analysis with  $k = 3$ . Cluster 1 is shown in blue and  
777 cluster 2 is shown in red, the third cluster associated with the image background has been set to  
778 white. *Right:* the spectra of cluster 1 and cluster 2 reconstructed from principal components  
779 compared to reference As standards. The sample is frozen-hydrated examined under the cryostream.  
780 Relative concentrations are depicted by shading with brighter colours equating to higher  
781 concentrations ('heatmap').

782

783

784

785

786

787 **TABLE CAPTIONS**

788

789 **Table 1.** Comparison of synchrotron X-ray methodological approaches that are available to an  
790 experimenter at XFM beamlines to interrogate As distribution and chemical speciation in *Pteris*  
791 *vittata* tissues. The exact values will change with the beamline.

792

793 **Table 2.** Bulk elemental concentrations in fronds of *Pteris vittata* (values as ranges and means in  $\mu\text{g}$   
794  $\text{g}^{-1}$  dry weight) with ICP-AES.

795

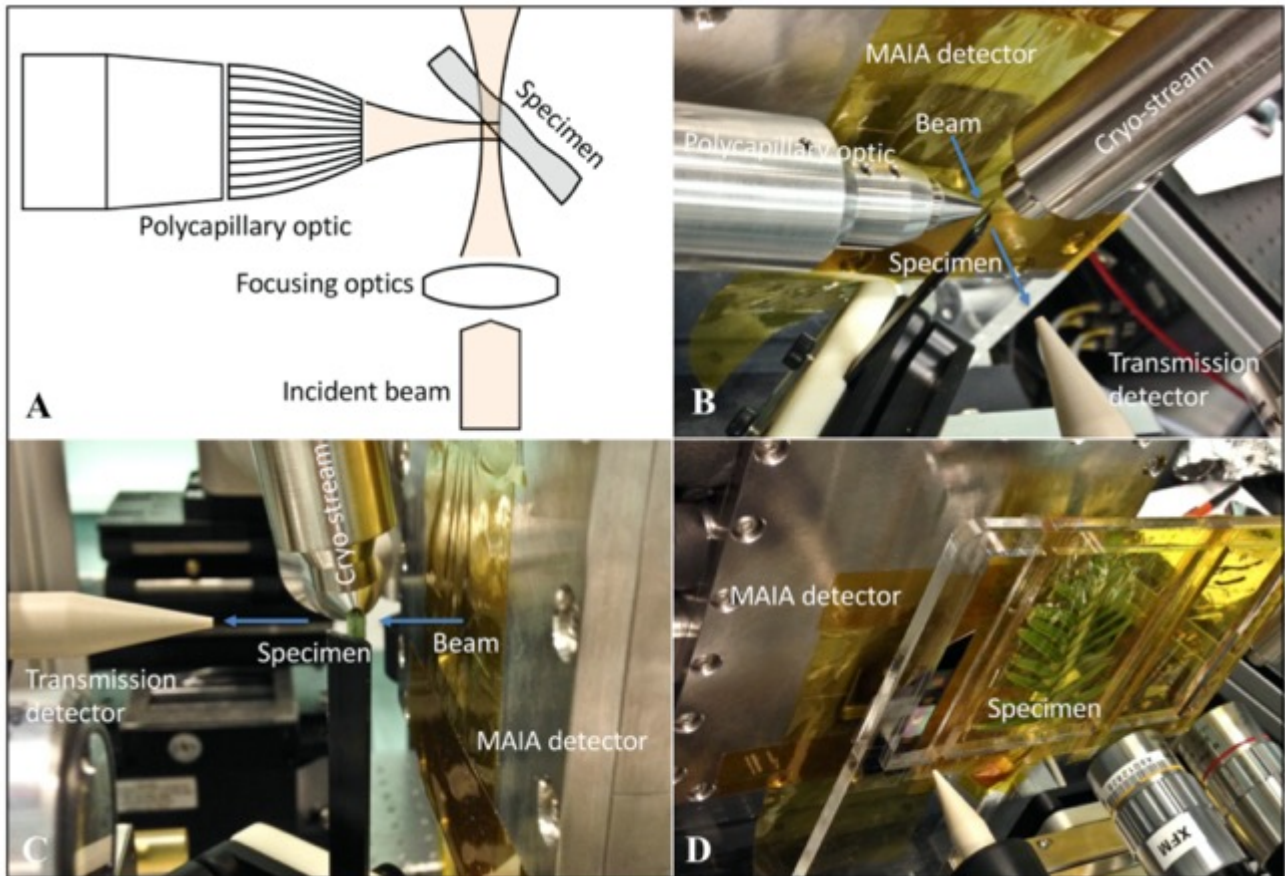
796

797 **Supporting Information**

798

799 Planar  $\mu$ XRF maps of As distribution in dehydrated *Pteris vittata* pinnule (Figure S1). Planar  $\mu$ XRF  
800 maps of As distribution in dehydrated *Pteris vittata* pinnule (Figure S2). Planar  $\mu$ XRF maps of As  
801 and K of a dehydrated cross-sectioned *Pteris vittata* pinnule (central portion) (Figure S3). Planar  
802  $\mu$ XRF maps of As and K of a dehydrated cross-sectioned *Pteris vittata* pinnule (Figure S4). Planar  
803  $\mu$ XRF maps of As and K of a dehydrated cross-sectioned *Pteris vittata* rachis (Figure S5). Planar  
804  $\mu$ XRF maps of the K, As, Zn and Compton signals of a dehydrated *Pteris vittata* pinnule margin  
805 (Figure S6). Planar  $\mu$ XRF maps of the K, As, Zn and Compton signals of a dehydrated *Pteris vittata*  
806 pinnule margin (Figure S7). Planar  $\mu$ XRF maps of the K, As, Zn and Compton signals of a  
807 dehydrated *Pteris vittata* pinnule margin (Figure S8). Confocal  $\mu$ XRF maps of As, Br, Ca and Rb in  
808 a freeze-dried *Pteris vittata* pinnule showing the varying degrees of self-absorption depending on  
809 element  $z$  (Figure S9). Confocal  $\mu$ XRF maps of As in *Pteris vittata* pinnule (terminal  
810 end/sporangium) (Figure S10). As fluorescence map from confocal  $\mu$ XRF imaging of *P. vittata*  
811 sporangia recorded using the Vortex SDD from an incident beam energy of 15.8 keV, showing the  
812 locations of the volumetric XANES measurements taken at the sporangia, As fluorescence map from  
813 confocal  $\mu$ XRF imaging of *P. vittata* midvein, volumetric XANES spectra taken from the ROIs  
814 identified (Figure S11). Supplementary Figure 12. As fluorescence map from confocal  $\mu$ XRF  
815 imaging of *P. vittata* sporangia, volumetric XANES spectra taken from the ROIs identified (Figure  
816 S12). Bright-field microscopy images of transversely cut sections of *Pteris vittata* samples (Figure  
817 S13).

818



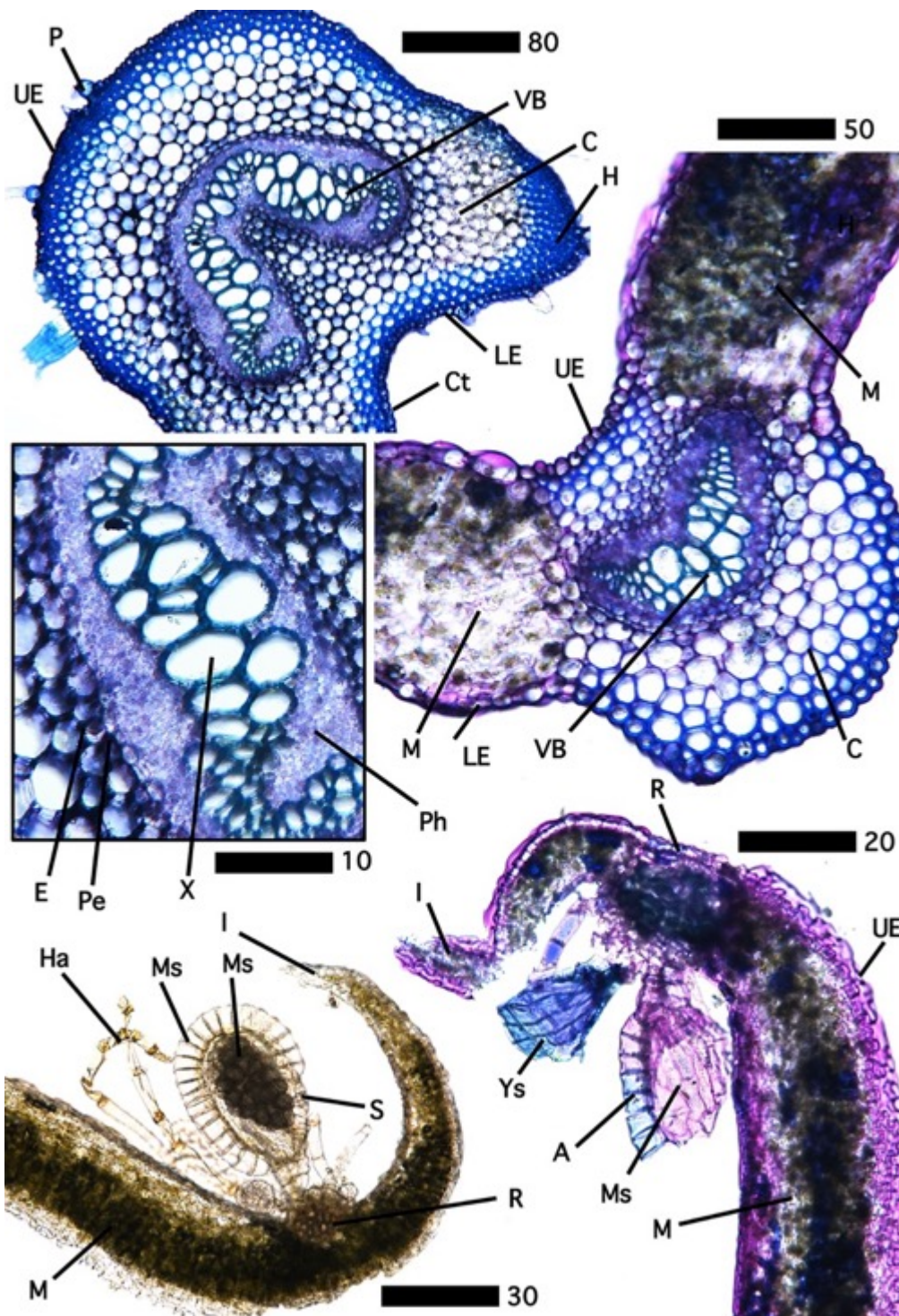
819

820

821 **Figure 1.** Experimental setup at the XFM beamline of the Australian Synchrotron: [A] Schematic  
 822 diagram of confocal probe, SDD – silicon drift detector (prepared by Gary Ruben) [B] frozen-  
 823 hydrated sample under the cryo-stream in front of the Maia detector; [C] Frozen-hydrated samples  
 824 probed with the confocal optic; [D] Maia planar imaging at room temperature of a large live frond  
 825 still attached to the plant (with rhizome in pouch with moist cotton). Typical dimensions of the probe  
 826 beam are  $\sim 1 \mu\text{m}$ , those of the confocal field of view are  $\sim 10 \mu\text{m}$ , and the specimen thickness is in the  
 827  $>100 \mu\text{m}$  domain.

828

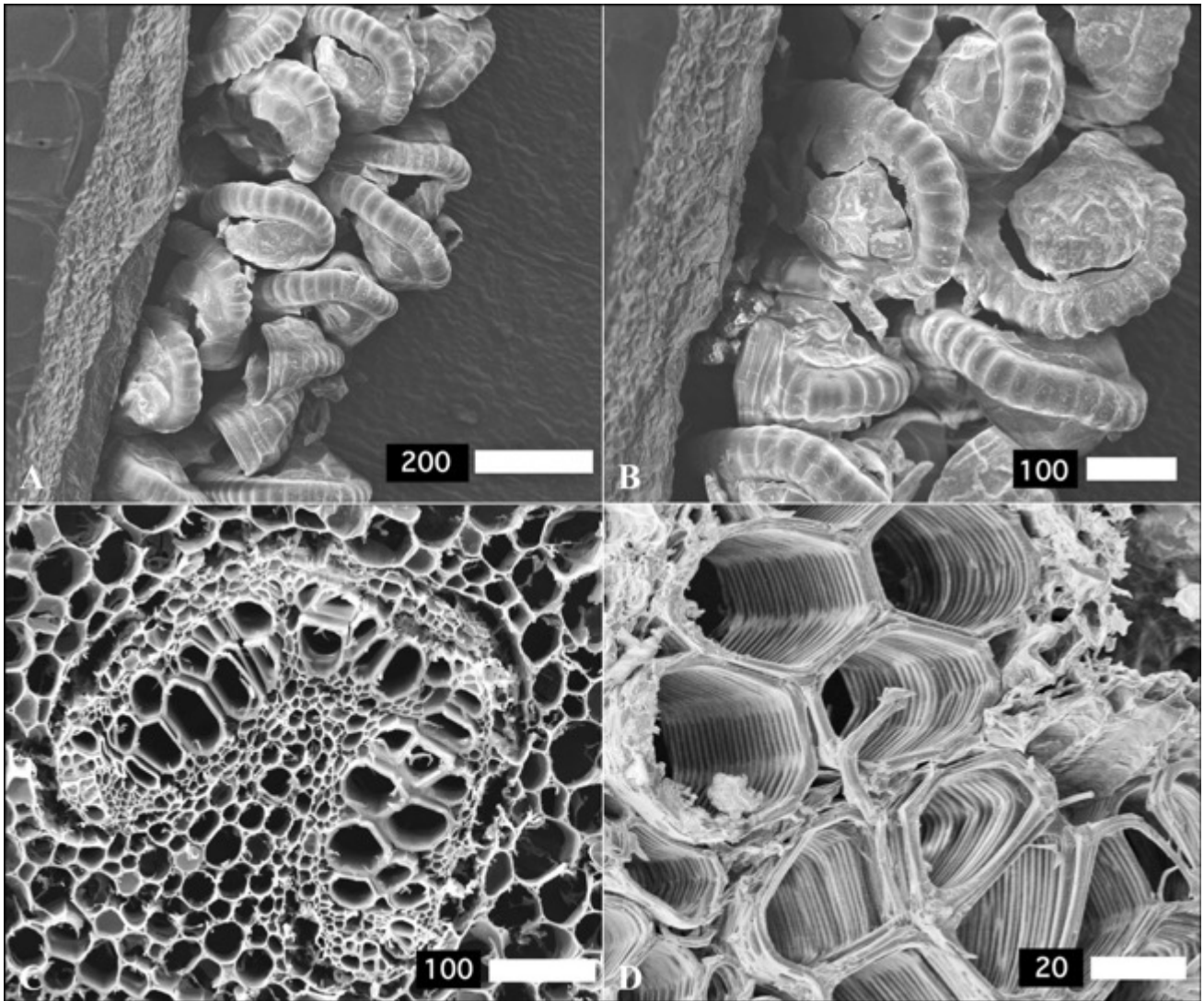
829



830

831

832 **Figure 2.** Toluidine blue stained *Pteris vittata* sections: [clockwise from top left] section of the  
 833 rachis; section of the central part of the frond; unstained and stained sections of the sporophytes  
 834 attached to the frond. Abbreviations: *LE* lower epidermis, *UE* upper epidermis, *C* cortex, *P* pamanta,  
 835 *VB* vascular bundle, *Ct* cuticle, *H* hypodermis, *M* mesophyll, *X* xylem, *E* endodermis, *Pe* pericycle,  
 836 *Ph* phloem, *R* receptacle, *I* false indusium, *Ha* hair, *Ys* young sporangium, *Ms* mature sporangium, *A*  
 837 annulus, *S* stomium. Scale bars denote μm.



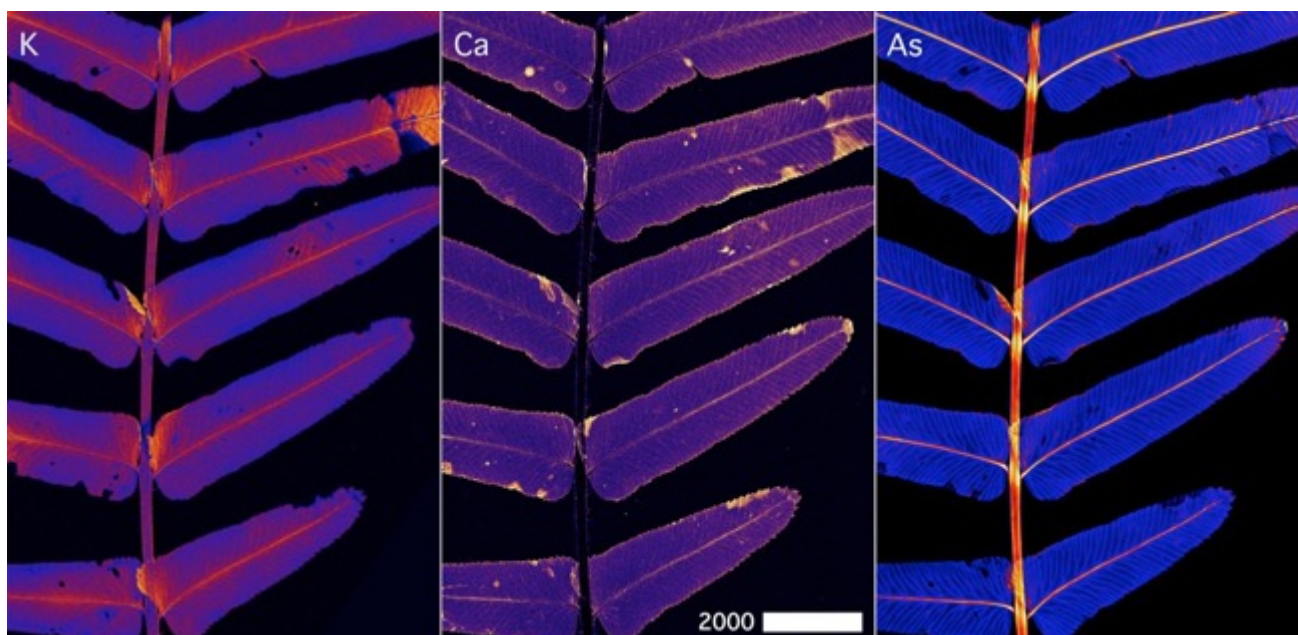
838

839

840 **Figure 3.** Scanning Electron Microscopy (SEM) images of *Pteris vittata* tissues: [A] sporangium  
841 enclosures within the margin of the frond (indusium); [B] detail of sporophytes showing [C] vascular  
842 bundles of the rachis; [D] detail of central xylem bundles. Scale bars denote μm.

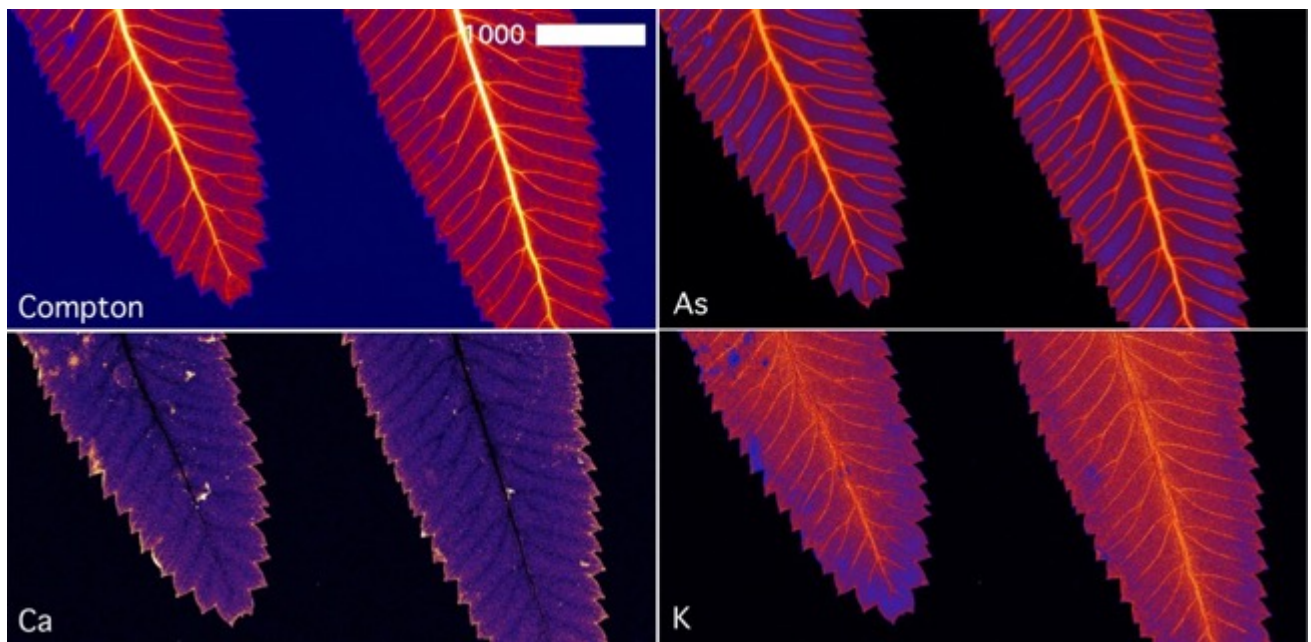
843

844



845  
846  
847  
848  
849  
850  
851

**Figure 4.** Planar  $\mu$ XRF maps of Ca, K and As of a live *Pteris vittata* of a partial frond with pinnae examined at room temperature. Relative concentrations are depicted by shading with brighter colours equating to higher concentrations ('heatmap'). Scale bars denote  $\mu\text{m}$ .



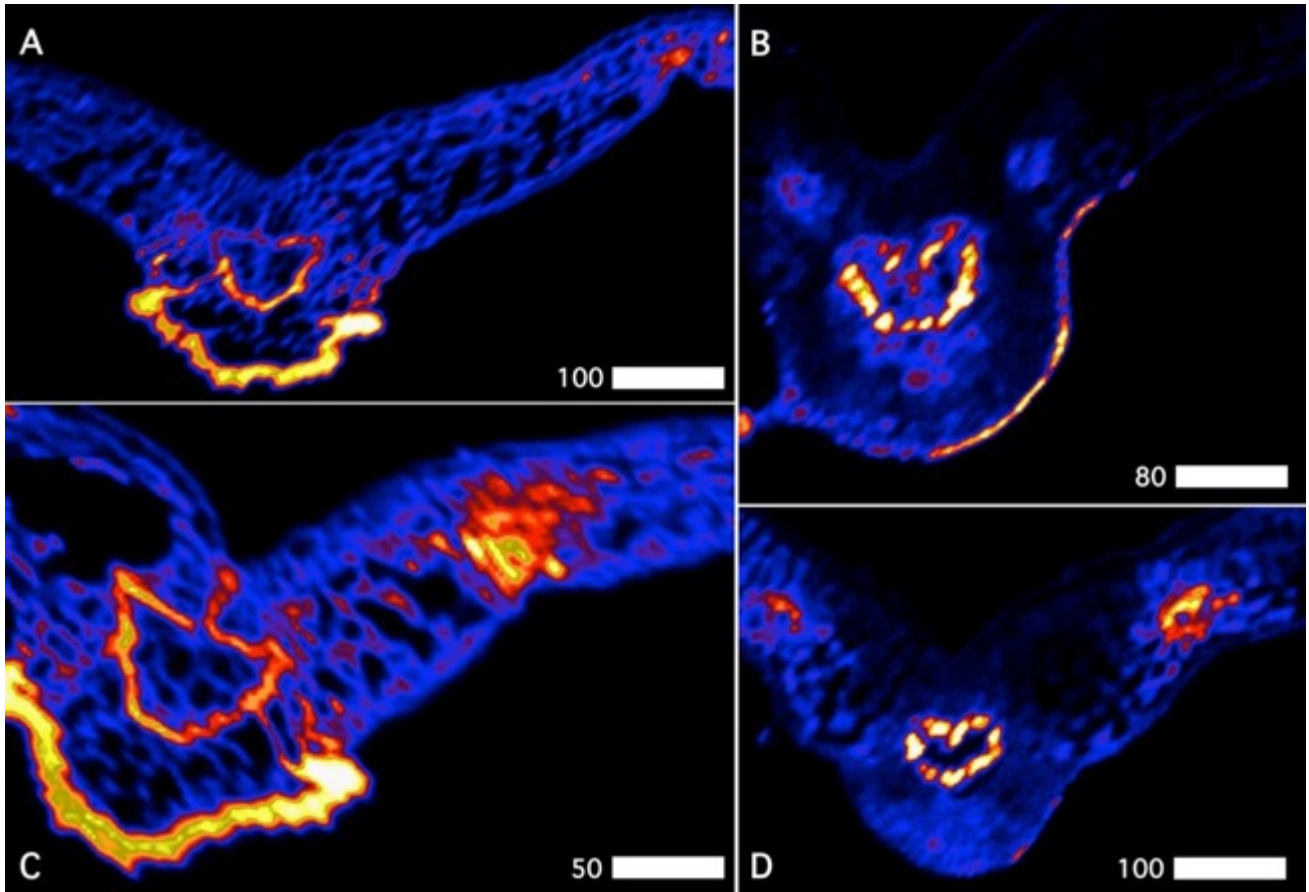
852

853

854 **Figure 5.** Planar  $\mu$ XRF maps of Ca, K, As and Compton Scatter of the terminal ends of a live *Pteris*  
855 *vittata* pinnules examined at room temperature. Relative concentrations are depicted by shading with  
856 brighter colours equating to higher concentrations ('heatmap'). Scale bars denote  $\mu$ m.

857

858



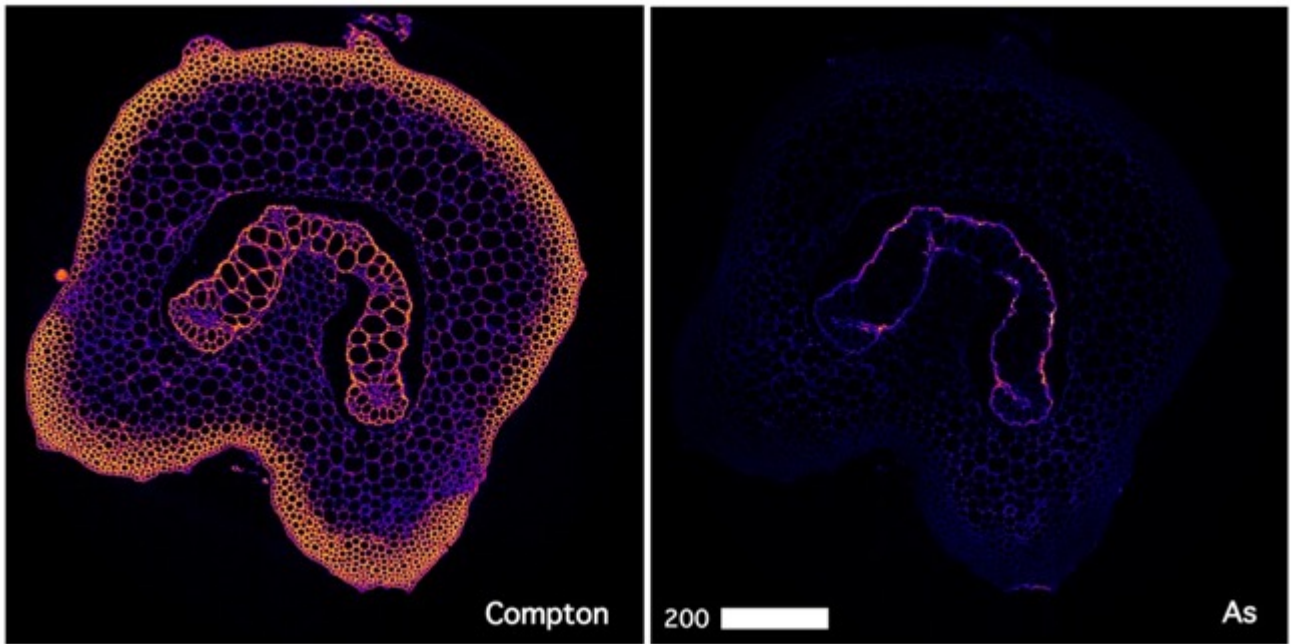
859

860

861 **Figure 6.** Confocal  $\mu$ XRF virtual section elemental maps of As in *Pteris vittata* pinnules (central  
 862 part/rachis). Panels: **[A]** freeze-dried f examined at room temperature; **[B]** frozen-hydrated examined  
 863 under the cryostream; **[C]** freeze-dried f examined at room temperature; **[D]** frozen-hydrated  
 864 examined under the cryostream. Relative concentrations are depicted by shading with brighter  
 865 colours equating to higher concentrations ('heatmap'). Scale bars denote  $\mu\text{m}$ .

866

867



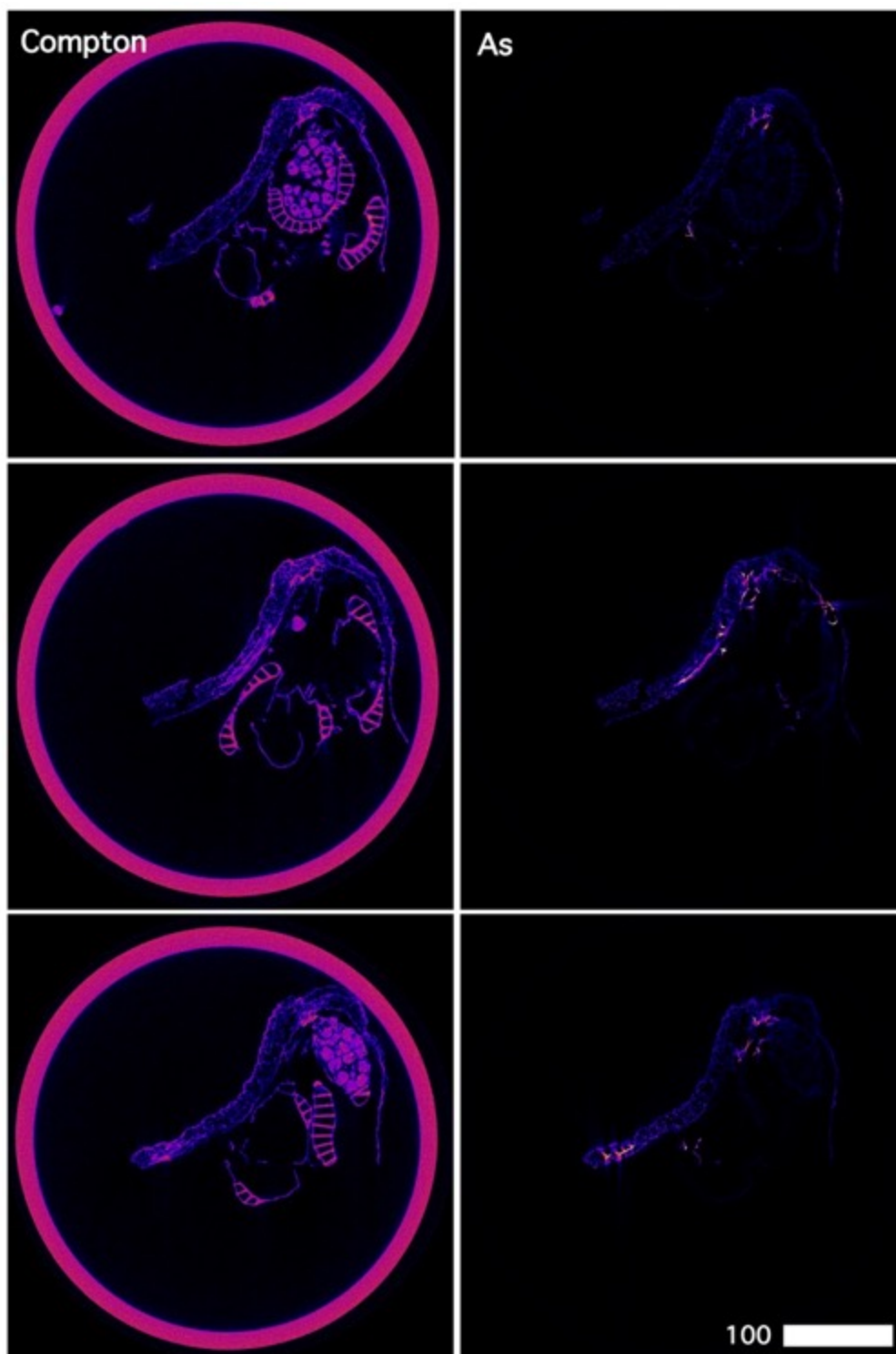
868

869

870 **Figure 7** Single-slice  $\mu$ XRF tomogram of a freeze-dried *Pteris vittata* rachis examined at room  
871 temperature showing As and Compton signals. Relative concentrations are depicted by shading with  
872 brighter colours equating to higher concentrations ('heatmap'). Scale bars denote  $\mu$ m.

873

874

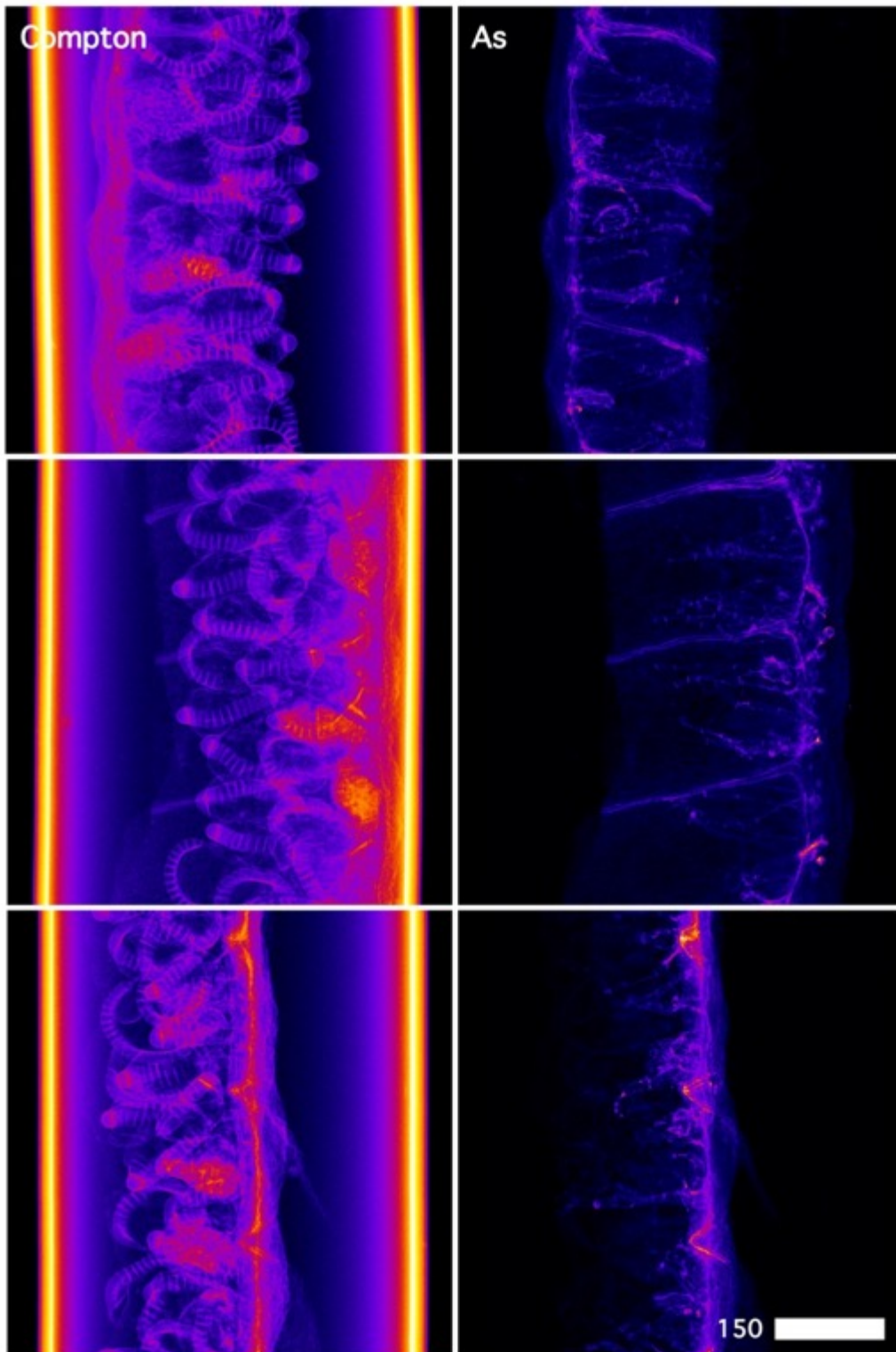


875

876

877 **Figure 8.** Single-slice  $\mu$ XRF tomograms of a freeze-dried *Pteris vittata* pinnule margin inside a  
 878 Kapton capillary examined at room temperature showing As and Compton signals. The same sample  
 879 at different depths is shown. Relative concentrations are depicted by shading with brighter colours  
 880 equating to higher concentrations ('heatmap'). Scale bars denote  $\mu\text{m}$ .

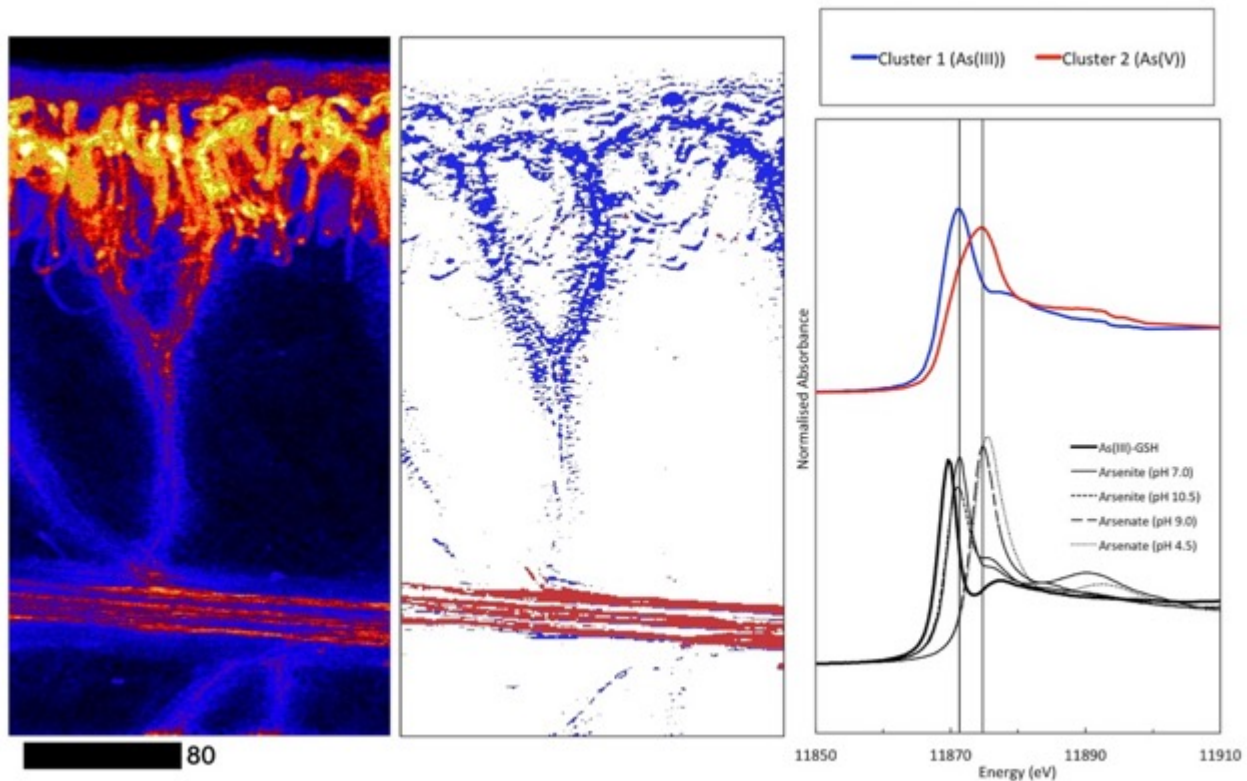
881



882

883

884 **Figure 9.** 2D  $\mu$ XRF maps of a freeze-dried *Pteris vittata* pinnule margin inside a Kapton capillary  
 885 examined at room temperature showing As and Compton signals from different angles. Relative  
 886 concentrations are depicted by shading with brighter colours equating to higher concentrations  
 887 ('heatmap'). Scale bars denote  $\mu$ m.



888

889

890 **Figure 10.** *Left:* As elemental map of a portion of *Pteris vittata* pinnule including midvein and leaf  
 891 margin, taken at the top energy of the 2D XANES imaging scan (12.1 keV). *Middle:* composite of  
 892 cluster maps generated by *k*-means clustering analysis with *k* = 3. Cluster 1 is shown in blue and  
 893 cluster 2 is shown in red, the third cluster associated with the image background has been set to  
 894 white. *Right:* the spectra of cluster 1 and cluster 2 reconstructed from principal components  
 895 compared to reference As standards. As the energy calibration of the standards was not performed at  
 896 the beamline, both cluster spectra have been shifted down in energy by 1 eV to align the peaks more  
 897 closely with those of the standards. The sample is frozen-hydrated examined under the cryostream.  
 898 Relative concentrations are depicted by shading with brighter colours equating to higher  
 899 concentrations ('heatmap'). Scale bars denote μm.

Analysis Type	Specimen preparation	Specimen state	Imaging Modality	X, Y, (Z) resolution [ $\mu\text{m}$ ]	Positive aspects	Negative aspects
$\mu\text{XRF}$	Sections	Dry or Frozen-hydrated	Projection imaging	2, 2, (30)	Fast acquisition Section thickness can match cellular length-scales	Disruptive preparation due to freeze-drying and/or sectioning
	Intact tissues	Frozen-hydrated	Projection imaging	2, 2, (none)	Fast acquisition Full specimen immobilisation	Narrow field of view depending on cryogenic implementation No depth information
	Intact tissues	Live hydrated	Projection imaging	0.5, 0.5, (none)	Fast acquisition Potential for sample evolution and degradation during analysis	Potential for radiation damage No depth information
	Intact tissues	Live hydrated / Dry	3D tomography	5, 5, 5	Ability to obtain 3D models of intact specimen	Potential for radiation damage Only for narrow specimen
	Intact tissues	Live hydrated / Dry	2D (single-slice) tomography	0.5, 0.5, 0.5	Acquisition of a single high-resolution virtual slice	Potential for radiation damage Only for narrow specimens
	Intact tissues	Frozen-hydrated	Confocal imaging	2, 2, 10	Direct access to internal volumes within extended specimens	Slower acquisition Increased radiation dose
XANES	--	--	XANES imaging	2, 2, (none)	Overall low radiation dose	No depth information
	--	--	Confocal XANES	2, 2, 10	Directly probes chemical speciation within internal volume	High radiation dose can result in photo-reduction

**Table 1.** Comparison of synchrotron X-ray methodological approaches that are available to an experimenter at XFM beamlines to interrogate As distribution and chemical speciation in *Pteris vittata* tissues. The exact values will change with the beamline.

Tissue	Origin	Sample preparation	As	Ca	Cu	Fe	K	Mg	Na	P	S	Zn
Pinnae	China	Freeze-dried	6130	4420	21	309	32 100	3650	3960	62 700	4410	93
Pinnae	China	Freeze-dried	8580	4620	29	281	33 000	4290	7190	55 000	4920	35
Pinnae	Cultured	Freeze-dried	777	6700	7.5	390	16 300	2620	1320	17 000	3070	28
Pinnae	Cultured	Freeze-dried	1130	10 300	8.3	203	12 300	3680	927	12 000	3100	40
Rachis	Cultured	Freeze-dried	1080	923	10	142	25 000	715	7702	37 600	1520	48
Rachis	Cultured	Freeze-dried	1350	924	10	171	24 300	682	7900	35 400	1440	34
Rachis	Cultured	Freeze-dried	1140	1620	8.2	145	27 300	1020	6570	34 200	2100	48
Rachis	China	Freeze-dried	4530	5760	16	313	24 900	4110	6740	67 000	3790	93
Whole frond	Cultured	Analysed living	5170	2180	15	152	33 000	2440	4440	27 300	2630	27

**Table 2.** Bulk elemental concentrations in fronds of *Pteris vittata* (values as ranges and means in  $\mu\text{g g}^{-1}$  dry weight) with ICP-AES.